A Daytime Complement to the Reverse Absorption Technique for Improved Automated Detection of Volcanic Ash

MICHAEL J. PAVOLONIS

Office of Research and Applications, NOAA/NESDIS, Madison, Wisconsin

WAYNE F. FELTZ

Cooperative Institute for Meteorological Satellite Studies, University of Wisconsin—Madison, Madison, Wisconsin

ANDREW K. HEIDINGER

Office of Research and Applications, NOAA/NESDIS, Madison, Wisconsin

GREGORY M. GALLINA

Washington Volcanic Ash Advisory Center, Satellite Analysis Branch, NOAA/NESDIS, Camp Springs, Maryland

(Manuscript received 20 September 2005, in final form 23 February 2006)

ABSTRACT

An automated volcanic cloud detection algorithm that utilizes four spectral channels (0.65, 3.75, 11, and 12 μm) that are common among several satellite-based instruments is presented. The new algorithm is physically based and globally applicable and can provide quick information on the horizontal location of volcanic clouds that can be used to improve real-time ash hazard assessments. It can also provide needed input into volcanic cloud optical depth and particle size retrieval algorithms, the products of which can help improve ash dispersion forecasts. The results of this new four-channel algorithm for several scenes were compared to a threshold-based reverse absorption algorithm, where the reverse absorption algorithm is used to identify measurements with a negative 11–12-μm brightness temperature difference. The results indicate that the new four-channel algorithm is not only more sensitive to the presence of volcanic clouds but also generally less prone to false alarms than the standard reverse absorption algorithm. The greatest impact on detection sensitivity is seen in the Tropics, where water vapor can often mask the reverse absorption signal. The four-channel algorithm was able to detect volcanic clouds even when the 11–12-μm brightness temperature difference was greater than +2 K. In the higher latitudes, the greatest impact seen was the significant reduction in false alarms compared to the reverse absorption algorithm and the improved ability to detect optically thick volcanic clouds. Cloud water can also mask the reverse absorption signal. The four-channel algorithm was shown to be more sensitive to volcanic clouds that have a water (ice or liquid water) component than the reverse absorption algorithm.

1. Introduction

Many previous articles and reports have described, in detail, the need to accurately identify the presence of volcanic ash in the atmosphere in a timely manner as a matter of aviation safety (e.g., Tupper et al. 2004; Tupper and Kinoshita 2003; Hufford et al. 2000). It is well known that volcanic aerosols can have serious aviation and human health impacts. This is not only true of areas immediately surrounding an erupting volcano because ash is often found to be present even thousands of kilometers away from the source volcano. Miller and Casadevall (2000) describe a number of dangerous, near tragic, and costly aircraft encounters with volcanic ash clouds. Direct human observations of volcanic clouds from the ground or air are very limited, so observations from satellite are greatly relied on. The multispectral image enhancement techniques of Ellrod et al. (2003), Ellrod (2004), and Ellrod and Schreiner (2004) have been used by Volcanic Ash Advisory Cen-

Corresponding author address: Dr. Michael Pavolonis, 1225 W. Dayton St., Madison, WI 53706.
E-mail: mpav@ssec.wisc.edu

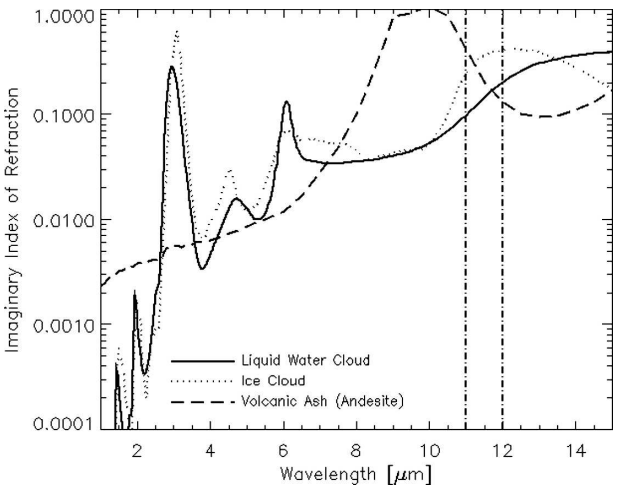

FIG. 1. The imaginary index of refraction of liquid water (solid line), ice (dotted line), and volcanic ash (andesite; dashed line) as a function of wavelength. The dash–dot lines intersect the three curves at 11 and 12 μm.

ters (VAACs) to aid in the manual identification of volcanic ash. Furthermore, a few automated algorithms have been presented in the literature. Higurashi and Nakajima (2002) used four channels in the 412–865-nm region to identify volcanic clouds that contained sulfate aerosols using Sea-Viewing Wide Field-of-View Sensor (SeaWiFS) data. Bonfiglio et al. (2005) and Pergola et al. (2004) presented an automated change-detection scheme that looks for anomalies in Advanced Very High Resolution Radiometer (AVHRR) radiances. This technique, while effective, requires a few years of training data for each region that is to be monitored.

The most commonly used satellite-based ash detection technique is often referred to as the "reverse absorption" technique (Prata 1989a,b). The physical basis of the reverse absorption technique, which uses brightness temperatures in the 11- and 12-μm region of the spectrum, can be elucidated by examining the imaginary index of refraction (m_i) of volcanic ash (Pollack et al. 1973), which is plotted as a function of wavelength in Fig. 1. Additional details concerning the m_i of ash will be discussed in section 2. The imaginary refractive indexes for water (from Downing and Williams 1975) and ice particles (from Warren 1984 and Gosse et al. 1995) are also shown. The imaginary index of refraction is directly proportional to absorption/emission strength for a given species composition and particle distribution, in that larger values are indicative of a stronger absorption of radiation at a particular wavelength. From Fig. 1 it is clear that ash will absorb more strongly at 11 μm than at 12 μm, while the opposite is true for water and ice clouds. Thus, liquid water clouds, ice clouds, and clear sky (e.g., water vapor) are generally characterized by a positive 11-μm minus 12-μm brightness temperature difference (hereafter, BTD[11, 12]); a "pure" nonopaque volcanic ash cloud in a dry atmosphere will have a negative BTD[11, 12]. A threshold of around 0 K is generally used when the reverse absorption technique is used in an automated sense.

The reverse absorption technique is well understood and has been shown to be quite effective (e.g., Schneider et al. 1995). Because the technique is well understood, the limitations are also very well known and are consistent with the physical basis of the algorithm (Prata et al. 2001). These limitations, which are also summarized in Prata et al. (2001), are the following.

1) Strong surface-based temperature inversions can cause the BTD[11, 12] to be negative.
2) When viewing barren surfaces (e.g., deserts) under clear-sky conditions, the BTD[11, 12] can be negative. This also can be true when viewing certain nonvolcanic, mineral-based aerosols (e.g., dust).
3) Cloud tops that overshoot the tropopause can cause a negative BTD[11, 12] due to the stratospheric temperature inversion.
4) Instrument noise and channel misregistration may also cause a negative BTD[11, 12]. This effect is usually associated with very cold scenes and, at times, cloud edges.
5) Very thick ash clouds or ash plumes with nontrivial liquid water or ice contents will generally have a positive BTD[11, 12].
6) High water vapor burdens can mask the negative BTD[11, 12] signal when viewing an actual ash cloud. As might be expected, this occurs most often in the Tropics.

It is important to note that the above reverse absorption technique limitations largely apply when using the reverse absorption technique in a quantitative/automated sense, not necessarily for qualitative applications. For instance, even when the commonly sought negative BTD[11, 12] signal is absent, a carefully scaled image of that brightness temperature difference often shows contrast between a volcanic cloud and other features that an experienced analyst can identify. Also, Yu et al. (2002) proposed a moisture correction technique that can help offset the sixth limitation listed above. When developing the automated algorithm presented in this paper, our goal was to negate each of the above limitations as much as possible during the day by supplementing a form of the reverse absorption technique with additional spectral information that is commonly available on a large number of satellite imaging

instruments [such as the AVHRR, Japan's Multifunctional Transport Satellite (MTSAT-1R), the Geostationary Operational Environmental Satellite (GOES), the Moderate Resolution Imaging Spectroradiometer (MODIS), and the Spinning Enhanced Visible and Infrared Imager (SEVIRI)]. Even though more sophisticated algorithms are possible with imagers such as MODIS, SEVIRI, and in the future, with the Visible/Infrared Imager/Radiometer Suite (VIIRS) on the National Polar orbiting Operational Environmental Satellite System (NPOESS) and the Advanced Baseline Imager (ABI) on GOES-R, it is important to have an algorithm that can be applied nearly universally to all current imagers. After all, imagers such as the AVHRR, MTSAT-1R, and GOES-M through P are scheduled to be in orbit for at least the next 7–10 yr.

In summary, there are four main reasons why we believe that the development of this automated global algorithm is important.

l) Our algorithm is physically based and was developed to be globally applicable and to work on a large variety of imaging satellite instruments. This algorithm is not meant to be a substitute for qualitative techniques used by trained analysts, but we will show that this automated algorithm will generate complementary information on the location of ash that can be used to add confidence to VAAC reports. Furthermore, even very large eruptions may not be noticed immediately by analysts, especially if the eruption is unexpected and occurs in a data-sparse location. For instance, the very unexpected 10 May 2003 eruption of Anatahan in the Mariana Islands was not identified by the VAAC in Washington, D.C., until about 4 h after the main eruption, even though it was detectable by satellite. This was the first known historical eruption of Anatahan and there were no regular geological activity reports, as this volcano was largely considered to be inactive or extinct; the Washington VAAC had no reason to closely monitor this island on their routine visual scan of the satellite imagery of active volcanic regions. An automated algorithm, such as the one presented in this paper, would have alerted VAAC analysts to this eruption much sooner.
2) We will also show that this algorithm is effective for identifying ice clouds that may be contaminated with volcanic ash, which is often associated with explosive eruptions or low-level ash that was entrained into strong convective updrafts. Both are difficult to detect using current standard automated methods.
3) Information on the presence of ash is needed at the pixel level to perform particle size, optical depth, and height retrievals using the most appropriate models. This can only come from an automated detection system if the retrievals are to be performed in near real time. The retrieval of these parameters is important for modeling the dispersion of volcanic clouds.
4) This algorithm can be used as a starting point for developing more complex algorithms that utilize relatively uncommon spectral channels that are only available on a few current imagers, such as MODIS and SEVERI, and will be available on future instruments like VIIRS and GOES-R.

In this paper, the construction of the volcanic cloud detection algorithm will be explained in a complete and stepwise manner beginning with a discussion of the physical basis for each component of the algorithm, which is then supplemented with radiative transfer model simulations. The performance of the algorithm will then be evaluated by examining five case studies and by a comparison to results from a fixed threshold reverse absorption method. Finally, the "false alarm" rate of the algorithm will be approximated by analyzing an entire day of global satellite data.

2. Algorithm physical basis

Consistent with Yu et al. (2002) and other studies, volcanic ash was modeled as andesite mineral and the real and imaginary index of refraction were taken from Pollack et al. (1973). Unfortunately, updated optical properties for volcanic ash have not been published. Single scatter properties for ash were generated by assuming spherical particles and applying Mie calculations (Tsay and Stephens 1990) to a given particle size distribution. Even though volcanic aerosol particles are not spherical in shape (e.g., Riley et al. 2003; Munoz et al. 2004), non-spherical aerosol databases and scattering models were not readily available at the time of this work. In addition, the model simulations are only used to roughly characterize the expected spectral behavior of ash clouds compared to meteorological clouds, so the Mie calculations should be sufficient. The density of the andesite mineral was taken to be 2.6 g cm^{-3} (e.g., Neal et al. 1994). Mie calculations were performed at 36 wavelengths, corresponding to the band central wavelength of each MODIS channel, for three different log-normal distributions of andesite mineral. The effective radius (r_{eff}), which is defined as the ratio from the third to second moment of the size distribution (Hansen and Travis 1974), for the three size distributions is 0.33, 2.41, and 8.11 μm, respectively. The single scatter albedo (ssa) of volcanic ash for the three size distributions is

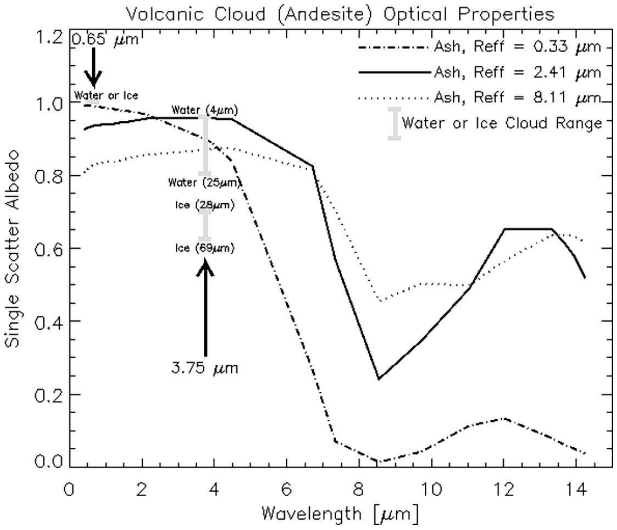

FIG. 2. The single scatter albedo as a function of wavelength for three lognormal size distributions of volcanic ash. A typical range in single scatter albedo for liquid water and ice clouds is also overlaid at 0.65 and 3.75 μm.

shown in Fig. 2 as a function of wavelength. The single scatter albedo can be interpreted as the probability that a photon will be scattered given an extinction event. Note that, analogously, (1.0 - ssa) can be interpreted as the probability of a photon being absorbed given an extinction event. The ssa for a large range of water (spherical droplets) and ice cloud r_{eff} (and habit for ice clouds) is also shown at the 0.65- and 3.75-μm wavelengths in Fig. 2. The ssa for water clouds was determined from Mie calculations and ssa was taken from Nasiri et al. (2002) for nonspherical ice crystals. The Nasiri et al. (2002) ice particle properties were determined from in situ measurements of cirrus clouds. Thus, the ice crystal distribution not only accounts for the variation in particle size but for habit as well.

It can be seen in Fig. 2 that the single scatter albedo is a strong function of particle size at wavelengths less than about 2 μm, with smaller particles having a greater probability of being scattered given an extinction event than large particles. At visible wavelengths ($\sim$0.65 μm), with the exception of very small ash particles (e.g., $r_{\text{eff}} = 0.33$ μm), the ssa of ash is significantly smaller than for water and ice clouds, which always have ssa values very close to unity. In the near-infrared, around 3.75 μm, both volcanic ash and water clouds will scatter photons more often than ice clouds. Volcanic ash and water clouds can often have similar single scatter albedos in the near-infrared. As at visible wavelengths, smaller particles tend to have larger ssa values than larger particles, regardless of the composition. One notable exception is associated with volcanic ash, in that the 2.41-μm (r_{eff}) distribution has the highest ssa followed by the 0.33- and 8.11-μm distributions. Using the information presented in Fig. 2 as a reference, assuming that the single scatter albedo is a fair predictor of the relative magnitude of the satellite-measured reflectance, and using m_i from Fig. 1, the following inferred properties can be used as the physical basis to develop a new automated volcanic ash detection technique.

l) The 0.65-μm visible reflectance R[0.65] of water and ice clouds of the same optical depth will almost always be greater than the R[0.65] of pure volcanic ash of the same optical depth. The only exception is when really fine ash is present (e.g., $r_{\text{eff}} < 0.5$ μm).
2) Water clouds and volcanic ash clouds of the same optical depth will often have similar reflectance values at 3.75 μm R[3.75], while both are more reflective than ice clouds of the same optical depth at 3.75 μm. Kinoshita et al. (2004) and Ellrod et al. (2003) also pointed out the potential usefulness of the 3.75-μm band for ash detection.
3) Thus, for a given optical depth, the ratio of R[3.75] to R[0.65] (hereafter RAT[3.75, 0.65]) for volcanic ash clouds will often be larger than RAT[3.75, 0.65] for water and ice clouds.
4) However, for a given cloud optical depth, the RAT[3.75, 0.65] for water clouds with small droplets (e.g., $r_{\text{eff}} < 4.0$ μm) and ash plumes may be very similar. This suggests that the edges of stratus and fair-weather cumulus clouds may have similar RAT[3.75, 0.65] values as some volcanic ash plumes. This is because the edges of liquid water clouds that are associated with small updrafts are generally characterized by small droplets due to evaporative processes.
5) Clouds with an 11-μm brightness temperature less than the homogeneous freezing point (233.16 K) and an R[3.75] that is typical of a water cloud are likely contaminated with aerosols (which are usually much smaller than ice crystals). Sherwood (2002) actually showed negative correlations between aerosol concentration (smoke and dust) from the Total Ozone Mapping Spectroradiometer (TOMS) and the reflective component of the 3.75-μm AVHRR channel associated with ice clouds. Tupper et al. (2005) used ice particle sized retrievals derived from 3.75-μm data to infer the presence of volcanic ash–contaminated cumulonimbi near Mount Pinatubo, Philippines, after the 15 June 1991 climatic eruption. Pyrocumulonimbi (e.g., Fromm and Servranckx 2003) may also cause an elevated R[3.75]. Thus, ice cloud pixels can be flagged as being contaminated with aerosol given a larger-than-expected R[3.75].

Furthermore, one would expect that very large contamination signals can only be caused by volcanic aerosols, which are more readily dispersed in larger concentrations and are generally more reflective at 3.75 μm than other aerosols. Yet ash-contaminated ice clouds can produce a signal similar to smoke- or dust- (nonvolcanic) contaminated ice clouds, especially if lower concentrations of low-level ash were transported to the upper troposphere by convective updrafts. Nevertheless, for aviation purposes, it may be desirable to avoid all detectable aerosol-contaminated clouds with glaciated tops, since even nonvolcanic dust can contain silicates that may be harmful to aircraft.

6) According to Sokolik and Toon (1999), the single scatter albedo of most mixed composition nonvolcanic dust samples were found to be >0.95 at 0.65 μm and <0.80 at 3.75 μm. Thus, given the information shown in Fig. 2, dust aerosols will tend to be less reflective at 3.75 μm and more reflective at 0.65 μm than volcanic ash, assuming neither are entrained in meteorological clouds. Furthermore, the higher in the atmosphere that the dust aerosol is, the greater the probability that it is volcanic in nature (as opposed to nonvolcanic dust) given that a volcanic eruption can provide a direct means of aerosol transport into the middle and upper troposphere in larger concentrations. This property can be roughly exploited in the algorithm by applying less strict 0.65- and 3.75-μm thresholds as the 11-μm brightness temperature of the target pixel decreases.
7) Figure 1 shows that volcanic ash is more absorbing in the 11-μm window region than either ice or liquid water. So, given a semitransparent ash cloud, an ice cloud, and a liquid water cloud of the same optical depth and thermodynamic temperature, the ash cloud will tend to have a lower 11-μm brightness temperature than either meteorological cloud (in the absence of a temperature inversion). This information is particularly useful when combined with the fact that the visible reflectance of the meteorological clouds referred to above will tend to be larger than the volcanic ash cloud visible reflectance.

3. Radiative transfer model simulations

Single scatter properties (single scatter albedo, asymmetry parameter, extinction coefficient) of andesite with an r_{eff} of 2.41 μm were used to perform radiance simulations for visible, near-infrared, and infrared channels with the radiative transfer model "Streamer" (Key and Schweiger 1998). More specifically, the radiative transfer calculations were performed for 4 channels by using the MODIS band weights for channel 1 (0.65 μm), channel 20 (3.75 μm), channel 31 (11 μm), and channel 32 (12 μm), although these results should also apply, at least qualitatively, to other sensors with very similar channels as well. Water and ice clouds were also simulated with "Streamer." Water clouds were taken to have spherical droplets with an effective particle radius of 10 μm. Nonspherical ice crystals were also simulated using single scatter properties (from Atmospheric Research Measurement (ARM) in situ measurements) taken from Nasiri et al. (2002). The chosen ice crystal distribution has an r_{eff} of 30.5 μm. Also, it has been shown by Rose et al. (1995, 2003), Guo et al. (2004), and others that ash plumes can often be mixed with ice and/or liquid water, so mixed liquid water/ash and ice/ash clouds were simulated by linearly combining optical properties as in Sun and Shine (1995) and Turner et al. (2003). The optical depth of each component of the cloud is used as a weight when calculating mixed cloud optical properties. This approach implies that the ash and water substance (liquid or ice) are mixed uniformly in the cloud. Of course, in reality, the mixed ash/water cloud may not consist of a uniform mixture and more complicated particle types such as ash encased in ice may be present. Recently published work by Textor et al. (2006a,b) has shown that ice/ash aggregates occur and can often be treated roughly as smaller pure ice particles (from a radiation perspective). Thus volcanic clouds composed of mainly aggregate ice/ash particles may also be characterized by an enhanced 3.75-μm reflectance as in Sherwood (2002) and Tupper et al. (2005), while our ice/ash and liquid water/ash mixture simulations are useful for roughly characterizing the effect of external cloud water/volcanic ash mixtures on measured satellite radiances. The visible optical depth of all types of clouds simulated was varied within the 0.01 to 50.0 range and calculations were performed for many different viewing and illumination angle configurations. The atmospheric profile was also varied in the simulations, but the cloud top pressure of the clouds simulated was kept constant. Ice clouds and ice/ash mixed cloud tops were positioned at 200 hPa and water clouds and water/ash mixed clouds at 700 hPa. Pure ash clouds were simulated twice, once at 200 hPa and again at 700 hPa. All calculations were performed assuming a water surface reflectance model based on Briegleb et al. (1986). When developing the ash detection algorithm, all of the simulations, covering a very large range of possible scenarios, were used; however, in this paper only a small subsample of those calculations are shown for the sake of clarity.

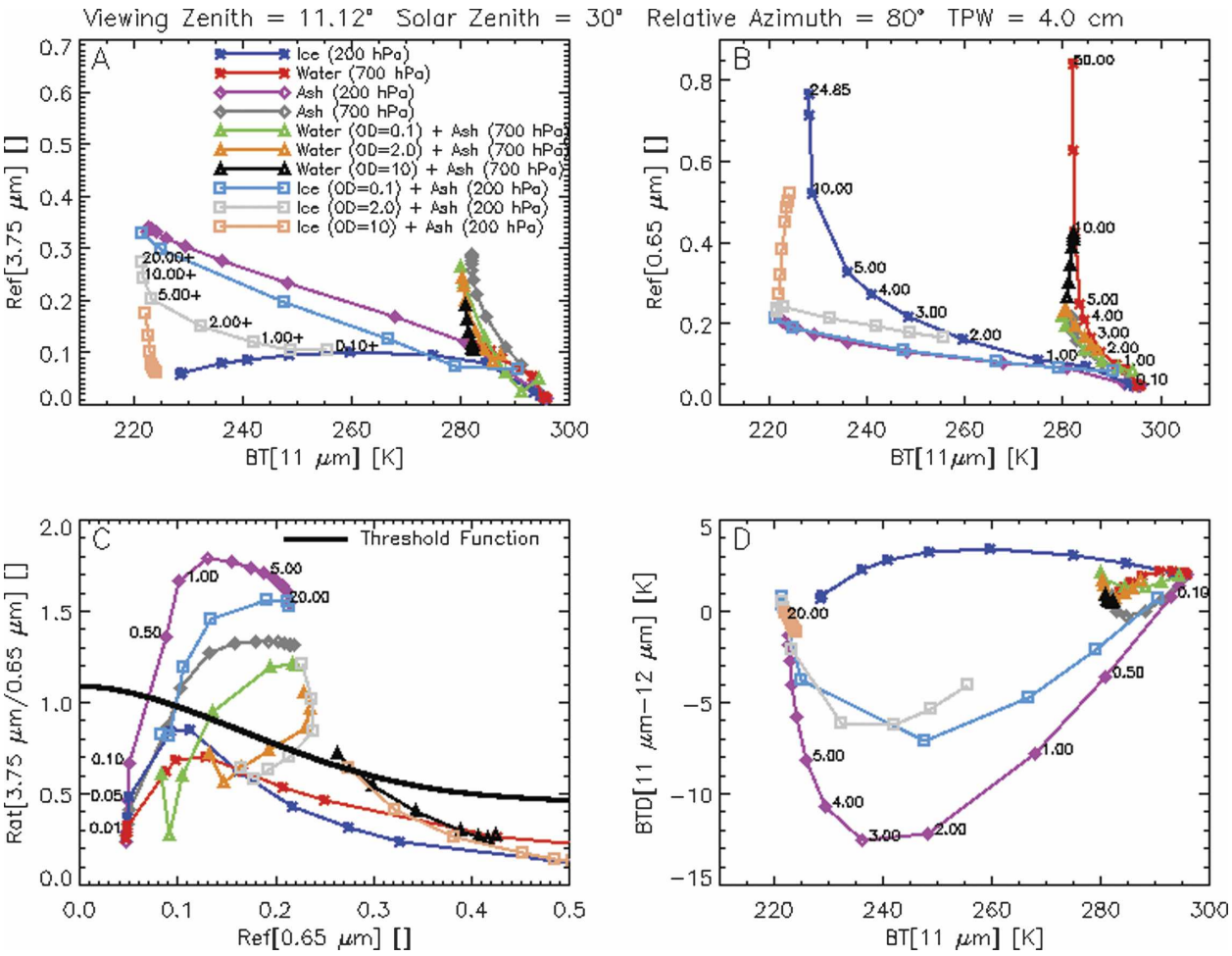

FIG. 3. Radiative transfer simulations for various types of meteorological and volcanic clouds. Each asterisk on the curves represents a new visible optical depth, some of which are labeled. The same optical depth combinations are shown on each panel. For the mixed ice/ash or liquid water/ash clouds, each curve represents a constant visible optical depth of the water component and the individual points on the curve represent a new optical depth for the ash component (plus the constant water component). The (a) 3.75-μm (in fractional form) and (b) 0.65-μm reflectance as a function of the 11-μm brightness temperature, (c) 3.75-/0.65-μm reflectance ratio as a function of the 0.65-μm reflectance, and (d) 11–12-μm brightness temperature difference as a function of 11-μm brightness temperature.

During the daytime, the radiance at 3.75 μm has both significant solar and thermal components. To obtain an estimate of the 3.75-μm reflectance due to the solar component, the contribution to the total radiance from thermal emission must be approximated and removed. As in Key and Intrieri (2000), Heidinger et al. (2004), and Pavolonis et al. (2005), the 3.75-μm reflectance estimate (R[3.75]) is calculated as shown in (1):

$$R[3.75] = \frac{L[3.75] - B(T[11])}{\mathrm{Lo}^{*}u - B(T[11])}, \qquad (1)$$

where $L[3.75]$ is the observed 3.75-μm radiance, $B(T[11])$ is the Planck function radiance at 3.75 μm that is calculated using the observed 11-μm brightness temperature, Lo is the solar constant for the 3.75-μm band (adjusted for earth-sun distance), and u is the cosine of the solar zenith angle.

Figure 3 shows the results of some of the radiative transfer simulations performed with a standard tropical atmospheric profile with a total precipitable water (tpw) of 4 cm and a viewing zenith angle of about 11°, a solar zenith angle of 30°, and a relative azimuth of 80°. In Fig. 3a, the simulated $R[3.75]$ is shown as a function of BT[11] for various visible optical depth configurations. Several curves are shown for the mixed clouds, where each curve represents a constant visible optical depth of the water component and the individual points on a curve represent a new visible optical depth for the

ash component (plus the constant water component). The simulations in Fig. 3a agree with the theory presented in Fig. 2, in that ice clouds that have a significant volcanic ash component will have a much larger R[3.75] than predicted for a pure ice cloud and a similar R[3.75] as a pure water cloud. We will assume that cloud water only exists in the form of ice when the BT[11] $<$ 243.0 K, although liquid water can exist at temperatures greater than 233.16 K if no ice nuclei are present. Thus, clouds without liquid water (e.g., BT[11] $<$ 243 K) that have an R[3.75] greater than some threshold ($\sim$0.1 in this case) can be taken to be contaminated with aerosols to some degree. For an external ice/ash mixture, the simulations indicate that the optical depth of the ash component should be roughly greater than or equal to the optical depth of the ice component for unambiguous detection. Figure 3a also shows that the R[3.75] may be useful for estimating the ratio of volcanic aerosol to ice present in the volcanic cloud, but that is not the focus of this paper.

Figure 3b shows R[0.65] as a function of BT[11] for the same cloud types shown in Fig. 3a. This figure further illustrates the notion presented in section 2 that a volcanic cloud of a given optical depth and height will be less reflective at 0.65 μm and less transmissive at 11 μm than a liquid water or ice cloud of the same optical depth and height. This also holds true of mixed clouds as long as the optical depth of the ash component is at least 1.0 and greater than or equal to the optical depth of the water component.

The information given by R[0.65] and R[3.75] can be combined into a ratio, R[3.75, 0.65], to provide additional quantitative information about the presence of volcanic ash. In Fig. 3c, the simulated R[3.75, 0.65] is shown as a function of R[0.65]. As expected, given the physical information contained in Fig. 2, the RAT[3.75, 0.65] of volcanic ash dominated clouds tends to be greater than the RAT[3.75, 0.65] of water or ice dominated clouds, where the volcanic ash signal is most pronounced when the R[0.65] is in the 0.09 (9%) to 0.35 (35%) range. Conversely, the RAT[3.75, 0.65] signal from meteorological clouds and ash clouds is most blurred when R[0.65] $<$ 0.09. Mixed clouds that are dominated by liquid water or ice cannot be unambiguously identified by this method (see black and beige curves). Of course, in strong sun glint conditions this approach will also not work well. In this work, a water pixel is taken to be in strong sun glint when the glint angle (Θ_{glint}) is $<$30°. The glint angle is defined as follows:

$$\Theta_{\text{glint}} = \cos^{-1}(\cos\theta_{\text{sun}}\cos\theta_{\text{sat}} + \sin\theta_{\text{sun}}\sin\theta_{\text{sat}}\cos\phi), \quad (2)$$

where θ_{sun} is the solar zenith angle, θ_{sat} is the satellite zenith angle, and ϕ is the relative azimuth angle. The treatment of pixels in sun glint will be discussed further in section 4, as will the threshold function shown in Fig. 3c.

Figure 3d shows BTD[11, 12] as a function of BT[11]. As expected, the BTD[11, 12] of pure ash clouds is highly dependent on the vertical location of the cloud due to differing water vapor absorption at 11 μm and 12 μm. The upper tropospheric ash cloud displays a significant negative BTD[11, 12] signal when the optical depth is greater than about 0.10. However, the lower tropospheric ash cloud only shows a very minor negative BTD[11, 12], in this tropical environment, when the optical depth is in the 1.0–5.0 range. When liquid water is added to the lower ash cloud, the negative BTD[11, 12] signal is lost. Further, we would expect the negative BTD[11, 12] signal for the lower ash cloud to be more pronounced in a drier atmosphere.

Mixed ice/ash clouds in the upper troposphere also tend to have a negative BTD[11, 12], which suggests that ice/ash eruptive clouds might be located in the lower stratosphere if a significant (e.g., $>$1 K) positive BTD[11, 12] is observed. Since absorption by water vapor in the infrared window is negligible above the upper troposphere, the actual magnitude of the positive BTD[11, 12] will depend on the variation of cloud emissivity with height and the amount of ice present relative to ash. This figure is also very intriguing in that it shows that the presence of ice can actually drive clouds with a small ash component (e.g., ash optical depth of 0.1) to have a significantly negative (e.g., <-3 K) BTD[11, 12] (see light gray curve), unlike pure ash clouds of the same ash optical depth (e.g., 0.10). The ice component acts to make the entire cloud less transmissive and hence less affected by lower tropospheric water vapor. However, pure ash clouds in the upper troposphere are shown to have a more negative BTD[11, 12] than all mixed ice/ash clouds when the optical depth of the pure ash cloud exceeds 0.5. In summary, these simulations highlight the complexities of using the reverse absorption technique alone to detect volcanic ash in an automated algorithm. The role of water in ash contaminated clouds is a very interesting and important topic that should be addressed further in future work.

4. Algorithm implementation

Since the new volcanic cloud detection algorithm described in this section uses data from four spectral channels, we will refer to the algorithm as the "four-channel algorithm." Four tiers of spectral tests and a very basic spatial filter compose the automated four-channel algorithm. These tiers will be discussed in the sections

below, after a word on the general philosophy used to develop thresholds associated with the various tests. Thresholds for each component of each test were initially developed from radiative transfer model simulations, some of which were presented in section 3. These thresholds were then adjusted, if needed, based on the analysis of many scenes as observed from satellite. Thus, even though only a single ash particle size distribution was assumed and only totally cloudy scenes were simulated (e.g., cloud edges were not simulated), the thresholds were adjusted and additional constraints were added, based on our extensive image analysis experience, to help account for these and other factors. In summary, simulations were used to define the expected behavior and shape of the threshold functions and the value of the individual threshold values, and comparisons with multispectral imagery were used to adjust the final threshold functions/values used in the algorithm.

Tiers I, II, and III are composed of tests designed to identify volcanic clouds. Tier I tests are designed to identify only the most unique volcanic ash signals. Tier II and tier III tests are less restrictive and will be more sensitive to both volcanic clouds and false alarms. Thus, tier I tests are subject to very few false alarms and tier III tests produce the most false alarms. Tier IV is composed of a series of restoral tests used to help filter out pixels that may have tested positive for volcanic ash but are not likely volcanic clouds. The restoral tests essentially combine various spectral information used in the tier I–III tests that helps to further characterize the differences between volcanic clouds and other features. In practice, tier I and tier II tests are applied to every pixel; if any of the tests in either tier are passed then the test for volcanic clouds is recorded as positive. Then, tier III tests are only applied to all pixels that are within 200 km of a pixel that tested positive for a volcanic cloud using at least one tier I test. Finally, tier IV tests are only applied to pixels that passed a tier II test and are not within 200 km of a pixel that tested positive using at least one tier I test. The 200-km area was chosen based on the analysis of many MODIS volcanic cloud scenes. In those MODIS scenes, the visible portion, as seen in true color imagery, of the various volcanic clouds generally extended no farther than about two hundred 1-km pixels in any direction. Of course, portions of volcanic clouds may be invisible in the imagery, but these clouds should not be detectable using our methods anyway. The various tiers of tests are discussed in more detail below.

a. Tier I tests

These tests are used to identify spectral signatures that are most uniquely associated with volcanic clouds. Based on the physical information presented in sections 2 and 3, unique volcanic cloud spectral signatures include one or more of the following characteristics: large and negative BTD[11, 12] values, large RAT[3.75, 0.65] values, and relatively low BT[11] values. The exact tests used, which are divided into three broad latitude bands, are listed in Table 1. Some comments describing the rationale for each test are also listed in Table 1. Note that nearly every test uses a form of the reverse absorption technique, which is supplemented with a BT[11] and RAT[3.75, 0.65] constraint. These constraints are very important for preventing false alarms. Reverse absorption false alarms will be discussed further in section 6. We applied these same tests to an entire day of global MODIS data that were known to be free of detectable volcanic clouds (see more on this in section 6) and found that less than 0.001% of pixels passed any of these tests, illustrating their truly unique nature.

b. Tier II tests

In tiers II (and III), three general types of tests are utilized: RAT[3.75, 0.65], BTD[11, 12], and REF[3.75] focused tests. The tier II tests are listed in Table 2. The RAT[3.75, 0.65] focused tests are the most useful for identifying volcanic ash clouds when the reverse absorption signal is obscured by water vapor. So these tests are the most useful for detecting optically thin ash clouds and volcanic ash clouds that reside in the lower and midtroposphere in moist environments. Even if there is a strong negative BTD[11, 12] signal, these tests provide redundant information that adds confidence to the detection results. When implementing the RAT[3.75, 0.65] tests, a dynamic RAT[3.75, 0.65] threshold is calculated as a function of R[0.65], as shown in Fig. 3c. The R[0.65] acts as a relative measure of cloud optical depth. Any observed RAT[3.75, 0.65] that is greater than the calculated threshold value is potentially associated with the presence of volcanic ash. To take into account viewing and illumination geometry, threshold functions are defined in 10° scattering angle bins. The scattering angle (Θ) is defined as

$$\Theta = \cos^{-1}[-1.0 \times (\cos\theta_{\text{sun}} \cos\theta_{\text{sat}} - \sin\theta_{\text{sun}} \sin\theta_{\text{sat}} \cos\phi)], \quad (3)$$

where θ_{sun} is the solar zenith angle, θ_{sat} is the satellite zenith angle, and ϕ is the relative azimuth angle. By this definition, angles less (greater) than 90° represent forward (backward) scattering.

The threshold function for each scattering angle bin is defined by a fourth degree polynomial that was initially fit to the radiative transfer model data and then adjusted slightly, based on the visual analysis of many

TABLE 1. A summary of the tier I tests used to identify pixels that contain a volcanic cloud. Tier I tests are applied to all qualified pixels (based on surface type). If any of these tests are true, then a volcanic cloud is present. These are the most strict tests and produce the most confident results. The tests are organized by latitude band. All of the symbols used are the same as those given in the text. All reflectance values are given in fractional form.

Region		Positive condition	Comments
30°S–30°N latitude	1	BT[11] $<$ 280 K	Cold cloud tops and nonvolcanic dust aerosols are screened out by using RAT[3.75, 0.65] condition.
	and	RAT[3.75, 0.65] $>$ 1.0	
	and	BTD[11, 12] $<$ 0.0 K	
	2	BT[11] $<$ 285 K	Some warmer pixels are allowed, but the BTD[11, 12] threshold is more strict.
	and	RAT[3.75, 0.65] $>$ 1.0	
	and	BTD[11, 12] $<$ −1.0 K	
	3	BT[11] $<$ 277 K	For colder pixels, the RAT[3.75, 0.65] constraint is lessened, but a more negative BTD[11, 12] is expected as well.
	and	RAT[3.75, 0.65] $>$ 0.7	
	and	BTD[11, 12] $<$ −2.0	
Not used over desert	4	BT[11] $<$ 233 K	Look for optically thick ice clouds that are heavily contaminated with smaller aerosol particles producing an uncharacteristically large REF[3.75] and reduced REF[0.65].
	and	REF[3.75] $>$ 0.20	
	and	REF[0.65] $<$ 0.60	
30°N(S)–60°N(S) latitude not used over desert	1	BT[11] $<$ 270 K	Similar tests as for the 30°S–30°N region, except a lower BT[11] threshold is generally used to prevent stratocumulus cloud decks from generating a true result. Also, since "cold" deserts (e.g., Gobi and Atacama) are located in this latitude region, the first two tests are not used over desert surfaces.
	and	RAT[3.75, 0.65] $>$ 1.0	
	and	BTD[11, 12] $<$ −0.5 K	
Not used over desert	2	BT[11] $<$ 270 K	
	and	RAT[3.75, 0.65] $>$ 0.7	
	and	BTD[11, 12] $<$ −1.0 K	
	3	BT[11] $<$ 277 K	
	and	RAT[3.75, 0.65] $>$ 0.7	
	and	BTD[11, 12] $<$ −2.0	
	4	BT[11] $<$ 233 K	
	and	REF[3.75] $>$ 0.20	
	and	REF[0.65] $<$ 0.60	
60°N(S)–90°N(S) latitude	1	BT[11] $<$ 270 K	BT[11] and RAT[3.75, 0.65] thresholds are more strict since many more features will have a negative BTD[11, 12] in the high latitudes.
	and	RAT[3.75, 0.65] $>$ 1.1	
	and	BTD[11, 12] $<$ −0.5 K	
	2	BT[11] $<$ 277 K	No RAT[3.75, 0.65] constraint is used since concentrated clouds of nonvolcanic dust are not expected at these latitudes.
	and	BTD[11, 12] $<$ −3.0 K	
	3	BT[11] $<$ 245 K	REF[3.75] threshold is more effective than RAT[3.75, 0.65] threshold over snow and ice.
	and	BTD[11, 12] $<$ −0.5 K	
	and	REF[3.75] $>$ 0.10	
	4	BT[11] $<$ 240 K	Nonvolcanic aerosol–contaminated ice clouds are less likely at high latitudes so a slightly higher BT[11] threshold is used.
	and	REF[3.75] $>$ 0.20	
	and	REF[0.65] $<$ 0.80	

scenes. The threshold functions used over water surfaces are the same as those used over land surfaces. This is because land surfaces are generally more reflective than water surfaces (excluding sun glint regions) at both 3.75 and 0.65 μm, so the R[3.75, 0.65] does not vary as much as the individual 3.75- and 0.65-μm reflectance values when viewing land scenes as opposed to water scenes. The coefficients needed to construct the dynamic R[3.75, 0.65] threshold functions are shown in Table 3.

TABLE 2. A summary of the tier II tests used to identify pixels that contain a volcanic cloud. Tier II tests are applied to all qualified pixels (based on surface type). If any of these tests are true, then a volcanic cloud is present. The tests are organized by surface type for each category. Note that the "Land" descriptor refers to nondesert land surfaces. All reflectance values are given in fractional form.

Category/surface		Positive condition	Comments
RAT[3.75, 0.65] dominated tests			
Water		RAT[3.75, 0.65] > dyn_thres + 0.1	Dyn_thres is the dynamic threshold determined as a function of REF[0.65] and geometry. BTD_THRES = 2.0, 1.0, and 0.5 K [20°S–20°N, 20°N(S)–45°N(S), 45°N(S)–90°N(S)]. This type of test is used to find volcanic cloud pixels that may not exhibit a negative BTD[11, 12] signal.
	and	BT[11] < 290 K	
	and	BTD[11, 12] < BTD_THRES	
	and	REF[0.65] > 0.06	
	and	REF[0.65] < 0.20	
	and	Glint angle > 30°	
Land		RAT[3.75, 0.65] > dyn_thres + 0.1	Dyn_thres is the dynamic threshold determined as a function of REF[0.65] and geometry. BTDJTHRES = 2.0, 1.0, and 0.5 K [20°S–20°N, 20°N(S)–45°N(S), 45°N(S)–90°N(S)].
	and	BT[11] < 290 K	
	and	BTD[11, 12] < BTD_THRES	
	and	REF[0.65] > 0.06	
	and	REF[0.65] < 0.40	
Desert		This category of test is not used over desert surfaces	
BTD[11, 12] dominated tests			
Land, water, and desert	1	BTD[11, 12] < −2.0 K	These two tests are designed to detect pure ash clouds. The RAT[3.75, 0.65] and REF[0.65] thresholds are used to filter out nonvolcanic dust pixels and clouds that reside in or above a temperature inversion.
	and	RAT [3.75, 0.65] > 0.95	
	and	REF[0.65] < 0.20	
	2	BTD[11, 12] < −0.5 K	
	and	RAT [3.75, 0.65] > 0.95	
	and	REF[0.65] < 0.10	
Land and water	1	BTD[11, 12] < −3.0 K	This test may be redundant at high latitudes given the tier I tests.
	and	BT[11] < 270 K	
	2	BTD[11, 12] < 0.0 K	By limiting this condition to pixels with BT[11] < 277 K, a less strict RAT[3.65, 0.65] constraint can be applied so that volcanic clouds with relatively large particles can be better detected, as the BT[11] threshold filters out most stratocumulus and nonvolcanic dust pixels.
	and	BT[11] < 277 K	
	and	RAT[3.75, 0.65] > 0.6	
	3	BTD[11, 12] < −0.5 K	Similar to the previous test except a more strict BTD[11, 12] test is used instead of a BT[11] constraint. Nonvolcanic dust may also exhibit this signature, but the restoral tests listed in Table 5 are used as a filter. The restoral tests work best in the Tropics, so this test is only used in the deep Tropics.
	and	RAT[3.75, 0.65] > 0.6	
	and	−20° < latitude < 20°	
REF[3.75] dominated tests			
Land, water, and desert	1	Ref[3.75] > 0.18	Look for an ice cloud that is contaminated with small particles.
	and	BT[11] < 235 K	
	2	Ref[3.75] > 0.08	A much less strict REF[3.75] threshold can be applied if a lower BT[11] threshold and an REF[0.65] constraint are used.
	and	BT[11] < 210 K	
	and	REF[0.65] < 0.40	

TABLE 3. The coefficients needed to calculate RAT[3.75, 0.65] thresholds as a function of REF [0.65] for 13 scattering angle bins. The threshold is calculated as follows: threshold = A*(REF [0.65])^4 + B*(REF[0.65])^3 + C*(REF[0.65])^2 + D*REF[0.65] + E. Scattering angles <50° generally do not occur so they are not included in the table. The REF[0.65] must be in fractional form.

Scattering angle (degrees)	A	B	C	D	E
50–60	−1.56E + 001	2.72E + 001	−1.03E + 001	−2.85E + 000	1.89E + 000
60–70	−3.48E + 001	6.01E + 001	−3.23E + 001	3.96E + 000	1.05E + 000
70–80	−2.99E + 001	4.53E + 001	−2.13E + 001	1.39E + 000	1.19E + 000
80–90	−2.29E + 001	4.09E + 001	−2.18E + 001	1.96E + 000	1.14E + 000
80–100	−5.25E + 001	8.02E + 001	−3.91E + 001	5.12E + 000	9.11E − 001
100–110	−9.09E + 001	1.27E + 002	−5.65E + 001	7.20E + 000	8.40E − 001
110–120	−5.48E + 001	7.87E + 001	−3.62E + 001	4.37E + 000	9.24E − 001
120–130	−5.47E + 001	7.48E + 001	−3.15E + 001	2.95E + 000	1.02E + 000
130–140	−5.63E + 001	7.31E + 001	−2.85E + 001	2.03E + 000	1.04E + 000
140–150	−5.01E + 001	6.32E + 001	−2.27E + 001	6.33E − 001	1.11E + 000
150–160	−3.08E + 001	3.92E + 001	−1.43E + 001	−5.59E − 002	1.12E + 000
160–170	−2.22E + 001	2.68E + 001	−8.09E + 000	−1.29E + 000	1.17E + 000
170–180	−2.03E + 001	2.18E + 001	−3.85E + 000	−2.43E + 000	1.26E + 000

To reduce false alarms, the RAT[3.75, 0.65] dynamic test is supplemented with additional spectral information. For instance, over water, the dynamic R[3.75, 0.65] threshold function is taken to be valid only for the following range in R[0.65]: 0.06 (6%) < R[0.65] < 0.20 (20%). This helps reduce false alarms caused by cloud edges and optically thick water clouds composed of small droplets. A positive BTD[11, 12] threshold is also used to minimize false alarms caused by cloud edges. To help avoid surface-induced false positives and nonvolcanic dust, the BT[11] must be <290 K. Strong sun glint regions are also ignored (e.g., $\Theta_{\text{glint}} < 30°$). If these conditions are met, ash is determined to be present. Table 3 provides a summary of the tier II RAT[3.75, 0.65] tests.

The second type of test used in tier II (and III) exploits BTD[11, 12] signals, and these tests may, at times, provide for some redundancy with the RAT[3.75, 0.65] focused tests. BTD[11, 12] tests largely utilize static thresholds and are the most useful for detecting volcanic clouds that reside in the upper troposphere or for detecting volcanic clouds that are in a dry atmosphere, as is typical of the high latitudes. Yet unlike the common implementation of the reverse absorption technique, constraints from additional spectral channels are applied in order to reduce false alarms. These constraints, which were chosen based on the spectral properties discussed in sections 2 and 3, largely prevent surface-based temperature inversions, nonvolcanic aerosols, and very high cloud tops from being falsely identified as volcanic ash. All of the BTD[11, 12]-based tests are summarized in Table 2.

The final type of tests used in tier II (and III) is designed to identify ice clouds that are potentially contaminated with volcanic ash and volcanic clouds that reside in the lower stratosphere or are very optically thick as a result of an explosive eruption. These tests generally provide more unique information than the RAT[3.75, 0.65] or BTD[11, 12] tests. The general premise is to look for very cold targets that have an REF[3.75] that is larger and an REF[0.65] that is smaller than would typically be expected for pure optically thick ice clouds. The RAT[3.75, 0.65] is not used as the main diagnostic because using the REF[3.75] and the REF[0.65] separately allows for a wider range of scenarios for these cold targets than the RAT[3.75, 0.65] alone. All of the REF[3.75] tests are summarized in Table 3. Pixels that pass any of the REF[3.75] tests are given a separate classification in the ash mask product called ash/ice. The exact meaning of this category is subject to further review in future work, as it is possible that an ice/SO_2/H_2SO_4 combination may also trigger one of these tests; so can pure, opaque ash clouds. Nevertheless, pixels that fall under this classification are generally filled with ice clouds that are heavily contaminated with aerosols. Nonvolcanic aerosols may cause this effect, but usually on a much smaller scale and with a signal that is much weaker (see discussion in section 2).

c. Tier III tests

Tier III tests, which are only applied to pixels that are within 200 km of a pixel that passed at least one tier I test, are conceptually similar to tier II tests. The main difference is that much less conservative thresholds are applied to these pixels and the RAT[3.75, 0.65] is used in sun glint regions as long as the BT[11] < 293.0. The use of these tests leads to both an increase in ash detection capabilities and, sometimes, false alarms. That is why they are only applied to regions where there is a

high confidence that a volcanic cloud is present. False alarms associated with these tests are almost always caused by liquid water cloud edges and regions of strong sun glint. However, as will be shown in section 5, tier III tests improve detection capabilities more than they increase false alarms. All tier III tests are summarized in Table 4.

d. Tier IV tests

Tier IV tests are only applied to pixels that passed a tier II test and are not within 200 km of a pixel that tested positive using at least one tier I test. The main purpose of these restoral tests is to eliminate false positives caused by nonvolcanic aerosols, mainly dust. The physical premise of these tests is that nonvolcanic dust tends to be warmer in the infrared window, brighter in the visible, and less bright in the near infrared than volcanic ash. If any of these tests (which are described in Table 5) are passed, then that pixel cannot be classified as containing a volcanic cloud.

e. Spatial filter

Finally, a simple 10×10 pixel spatial filter is applied to the finished mask. Any positive volcanic cloud pixel that is not in a 10×10 pixel area with at least a 20% volcanic cloud fraction is reset to a negative result (e.g., no volcanic cloud). In addition, any positive volcanic cloud pixel that is in an area where 99% of the positive volcanic cloud pixels have a BT[11] $>$ 293 K and a BTD[11, 12] $>$ 1.9 K, which represents pixels that barely passed the RAT[3.75, 0.65] test in tier III, is reset to negative. This filter simply acts to eliminate scattered "noisy" pixels from the final product and to reduce the number of cloud edges falsely identified as volcanic cloud in the Tropics, where the RAT[3.75, 0.65] test is relied on the most. A more sophisticated filter can probably be developed to further eliminate false alarms. In addition, filters can also be used to help increase detection capabilities. For instance, fresh eruptive volcanic aerosol features with significant liquid water components, which are often termed volcanic plumes, may be better detected using a more aggressive RAT[3.75, 0.65] test for pixels located near thermal anomalies, which are often associated with active volcanoes. Nevertheless, our main focus in this work was to develop physically based spectral tests, not advanced image processing techniques.

f. Application to GOES-M and AVHRR/3

It is important to note that the GOES-M through GOES-P imagers will not have the 12-μm channel in order to have a 13.3-μm CO_2 absorption channel. Ellrod (2004), Ellrod and Schreiner (2004), and Fig. 1 indicate that it should be possible to substitute the 13.3-μm band for the 12-μm band in this algorithm, with some threshold adjustments. Although since the atmospheric weighting function of the 13.3-μm channel peaks in the mid- to upper troposphere, any sensitivity to ash plumes in the lower troposphere from this test may be lost. Furthermore, all AVHRR instruments beginning with (National Oceanic and Atmospheric Administration) *NOAA-15* have two near-infrared channels, 1.6 and 3.75 μm. Unfortunately, only one of those channels can be transmitted during daytime operations. Currently, with the exception of *NOAA-17*, the 3.75-μm channel is transmitted, so this algorithm cannot be applied to the AVHRR on *NOAA-17* at this time. However, *NOAA-17* and *Terra* (which has a MODIS instrument) are in very similar midmorning orbits. MODIS then, provides for some redundancy of this orbit, so that very little temporal coverage is lost when this algorithm is applied to the polar orbiting imaging instruments. The AVHRRs on *NOAA-12*, *-14*, *-15*, *-16*, *-17*, and *-18* are currently still functioning.

5. Algorithm performance

Four MODIS scenes and an AVHRR scene were chosen to qualitatively assess the performance of the algorithm. It is important to note that the algorithm was not tuned to these scenes. The volcanic ash mask results for each case are also compared to the results derived by using a simple threshold-based reverse absorption algorithm to help illustrate the impact of added spectral information on an automated algorithm. It is important to keep in mind that the reverse absorption technique alone often has significant qualitative value. So even when an automated quantitative version of the technique does not "detect" the volcanic cloud, an experienced analyst may be able to identify the plume using properly enhanced split window imagery. The threshold-based reverse absorption algorithm used here works as follows: ash is deemed to be present if the BTD[11, 12] $<$ 0.0 (-0.2) from 30°S to 30°N (elsewhere). This type of reverse absorption threshold approach was also used in Yu et al. (2002). The first two cases capture volcanic clouds associated with two of the numerous eruptions of Manam, located in Papua New Guinea (PNG), that began in earnest in October of 2004. The third scene shows a high-latitude volcanic cloud from Klyuchevskoy on the Kamchatka Peninsula, Russia, and the fourth case is taken from a 1-km AVHRR image of an August 1992 eruption of Mount Spurr, Alaska. Finally, in an effort to show that the new

TABLE 4. A summary of the tier III tests used to identify pixels that contain a volcanic cloud. Tier III tests are only applied to pixels that are within about 200 km of a pixel that passed at least one tier I test. If any of these tests are true, then a volcanic cloud is present. All reflectance values are given in fractional form.

Category/surface		Positive condition	Comments
RAT[3.75, 0.65] dominated tests			
Water		RAT[3.75, 0.65] > dyn_thres −0.1	Dyn_thres is the dynamic threshold determined as a function of REF[0.65] and geometry. BTD_THRES = 2.0 (0.7, if glint), 1.0 (0.0, if glint), and 0.5 K [20°S–20°N, 20°N(S)–45°N(S), 45°N(S)–90°N(S)].
	and	BT[11] < 295 K	
	and	BTD[11, 12] < BTD_THRES	
	and	REF[0.65] > 0.04	
	and	REF[0.65] < 0.30	
Land		RAT[3.75, 0.65] > dyn_thres −0.025	Dyn_thres is the dynamic threshold determined as a function of REF[0.65] and geometry. BTD_THRES = 2.0, 0.5, and 0.0 K [20°S–20°N, 20°N(S)–45°N(S), 45°N(S)–90°N(S)]. Note that the land thresholds are slightly different than the water thresholds.
	and	BT[11] < 295 K	
	and	BTD[11, 12] < BTD_THRES	
	and	REF[0.65] > 0.04	
	and	REF[0.65] < 0.40	
Land and water		RAT[3.75, 0.65] > 1.2	In the deep Tropics, this test, which does not rely on a BTD[11, 12] threshold, is useful for detecting low- and midlevel volcanic clouds in very moist environments. The BT[11] and REF[0.65] constraints help to reduce false alarms due to cloud edges.
	and	BT[11] < 283 K	
	and	REF[0.65] > 0.10	
	and	REF[0.65] < 0.20	
	and	−20° < latitude < 20°	
Desert		This category of test is not used over desert surfaces.	
BTD[11, 12] dominated tests			
Land and water	1	BTD[11, 12] < 0.0 K	These next two tests are similar to those listed in Table 2, except much looser thresholds are applied.
	and	BT[11] < 290 K	
	and	RAT[3.75, 0.65] > 0.5	
	2	BTD[11, 12] < 0.5 K	
	and	BT[11] < 290 K	
	and	RAT[3.75, 0.65] > 0.7	
	3	BTD[11, 12] < −0.2 K	This test was designed to be effective over snow/ice surfaces. The RAT[3.75, 0.65] < 0.2 condition is used to filter out liquid water–dominated clouds and the REF[3.75] condition is used to filter out clear snow/water surface signatures and ice clouds.
	and	RAT[3.75, 0.65] < 0.2	
	and	REF[3.75] > 0.03	
	and	Latitude is poleward of 50°	
	and	Viewing angle <50°	
REF[3.75] dominated tests			
Land, water, and desert	1	REF[3.75] > 0.06	All three of these tests are similar to those listed in Table 2, except the thresholds are much less strict.
		BT[11] < 210 K	
		REF[0.65] < 0.40	
	2	REF[3.75] > 0.06	
		BT[11] < 200 K	
		REF[0.65] < 0.50	
Land and water		REF[3.75] < 0.10	
		BT[11] < 243 K	
		REF[0.65] < 0.70	
		RAT[3.75, 0.65] > 0.2	

TABLE 5. A summary of the tier IV tests that are used to identify pixels that passed at least one tier II test but are characterized by certain spectral properties that are uncharacteristic of volcanic clouds. If any of these conditions are true, the volcanic cloud flag is reset to negative (no volcanic cloud). All reflectance values are given in fractional form.

Surface		Positive condition	Comments
Land and water	1	BT[11] > BT_THRES	Volcanic ash should not be "warm," "bright," and have a relatively small RAT[3.75, 0.65]. Pixels that pass any of these three tests are likely nonvolcanic dust or cloud edges.
		RAT[3.75, 0.65] < 0.70	
		REF[0.65] > 0.12	
	2	BT[11] > BT_THRES + 3.5 K	BT_THRES is a function of view angle (va).
		RAT[3.75, 0.65] < 0.85	BT_THRES = 285 (va < 45°), 283 (45° < va < 58°), and 282 K (va > 58°).
		REF[0.65] > 0.11	
	3	BT[11] > BT_THRES + 5.0 K	
		REF[0.65] > 0.10	
Water		Glint angle <30°	Screen out very warm pixels that reside in sun glint.
		BT[11] > 293 K	
Land		BT[11] > 280 K	Volcanic ash should not be bright in the visible, yet transmissive in the infrared.
		REF[0.65] > 0.20	

four-channel algorithm can differentiate between volcanic ash and nonvolcanic dust, a nonvolcanic mineral dust cloud produced by a storm over the Sahara Desert is analyzed. Table 6 lists specific information about the MODIS granules and AVHRR orbit used in this analysis. When MODIS data are used, a true color image can be created, where channel 1 (0.65 μm) reflectance is displayed on the red color gun, channel 4 (0.56 μm) reflectance is displayed on the green gun, and channel 3 (0.47 μm) reflectance is displayed on the blue gun. If the ash concentration is significant enough at a given location in the true color image, it will appear brown, which is generally in stark contrast to meteorological clouds, although ash-contaminated ice clouds may also appear white. Unfortunately, the channels needed to make true color images do not currently exist on any operational sensor, so this kind of imagery cannot be routinely used for volcanic ash detection at this time. We acknowledge that the true color imagery does not qualify as "truth," but it is one of the best diagnostic tools available. Also, since only the 0.65-μm channel is used in the new volcanic cloud detection algorithm, the true color images are a fairly independent source of information. Since the Mount Spurr case has been discussed extensively in the literature (e.g., Schneider et al. 1995; Simpson et al. 2000; Rose et al. 2001) and because true color images cannot be made with AVHRR data, only a channel 4 (10.8 μm) infrared image is shown for that scene. A BTD[11, 12] image is also shown for each case. Finally, the results of the reverse absorption algorithm and the four-channel algorithm are overlaid on separate images of each scene.

a. Scene 1: Manam, PNG (24 October 2004)

The first case was captured well by *Aqua* MODIS on 24 October 2004 at 0355 UTC. These Manam eruptions occurred in a very moist and cloudy environment. MODIS infrared retrievals (Seemann et al. 2003) estimated the clear sky total precipitable water to be in excess of 5.0 cm in the general vicinity of Manam for both cases. The eruptions from Manam also tend to be Strombolian in style, which results in volcanic clouds that contain less fine ash (A. Tupper 2006, personal communication). The reverse absorption technique is most sensitive to the presence of fine ash. Focusing on the first Manam case, which is shown in Fig. 4, it is clear that this is a very complex scene in that it appears that both ash and meteorological clouds, at times, coexist in the same MODIS field of view. The fixed threshold reverse absorption technique is only able to detect a small portion of the core of the volcanic cloud, while the new four-channel algorithm is able to successfully identify nearly all of the volcanic cloud that is not totally obscured by overlying cirrus cloud. Note that the BTD[11, 12] is generally >1.0 K away from the volcanic cloud core. This lower volcanic cloud was estimated to have a maximum height of about 5600 m by the Darwin VAAC (see online at http://www.bom.gov.au/info/vaac/advisories.shtml). The new algorithm also flags a large region next to the main ash cloud as being an ice cloud that is contaminated by volcanic aerosol. This result cannot be verified simply by analyzing the true color image, so independent Atmospheric Infrared Sounder (AIRS) data were consulted. AIRS is a high spectral resolution grating spectrometer with thousands of

TABLE 6. Details of the five satellite-based case studies presented in this study.

Scene	Sensor	Date	Time (UTC)
Manam, PNG	*Aqua* MODIS	24 Oct 2004	0355
Manam, PNG	*Terra* MODIS	29 Nov 2004	0040
Klyuchevskoy, Russia	*Terra* MODIS	8 Mar 2005	0055
Mount Spurr, Alaska	*NOAA-11* AVHRR	19 Aug 1992	0126
East Atlantic Saharan dust	*Aqua* MODIS	16 May 2005	1420

channels in the 3.7–15.4-μm range. The AIRS is also located on the *Aqua* platform. AIRS SO_2 imagery obtained online (available at http://toms.umbc.edu; not shown) indicates that this ice cloud region is characterized by a very large SO_2 signal typical of a volcanic cloud. The reverse absorption technique produces scattered false alarms associated with convective clouds while the four-channel algorithm produces no noticeable false alarms.

b. Scene 2: Manam, PNG (29 November 2004)

The second Manam case was viewed by *Terra* MODIS on 29 November 2004 at 0040 UTC. This scene, shown in Fig. 5, is less complex than the 24 Oc-

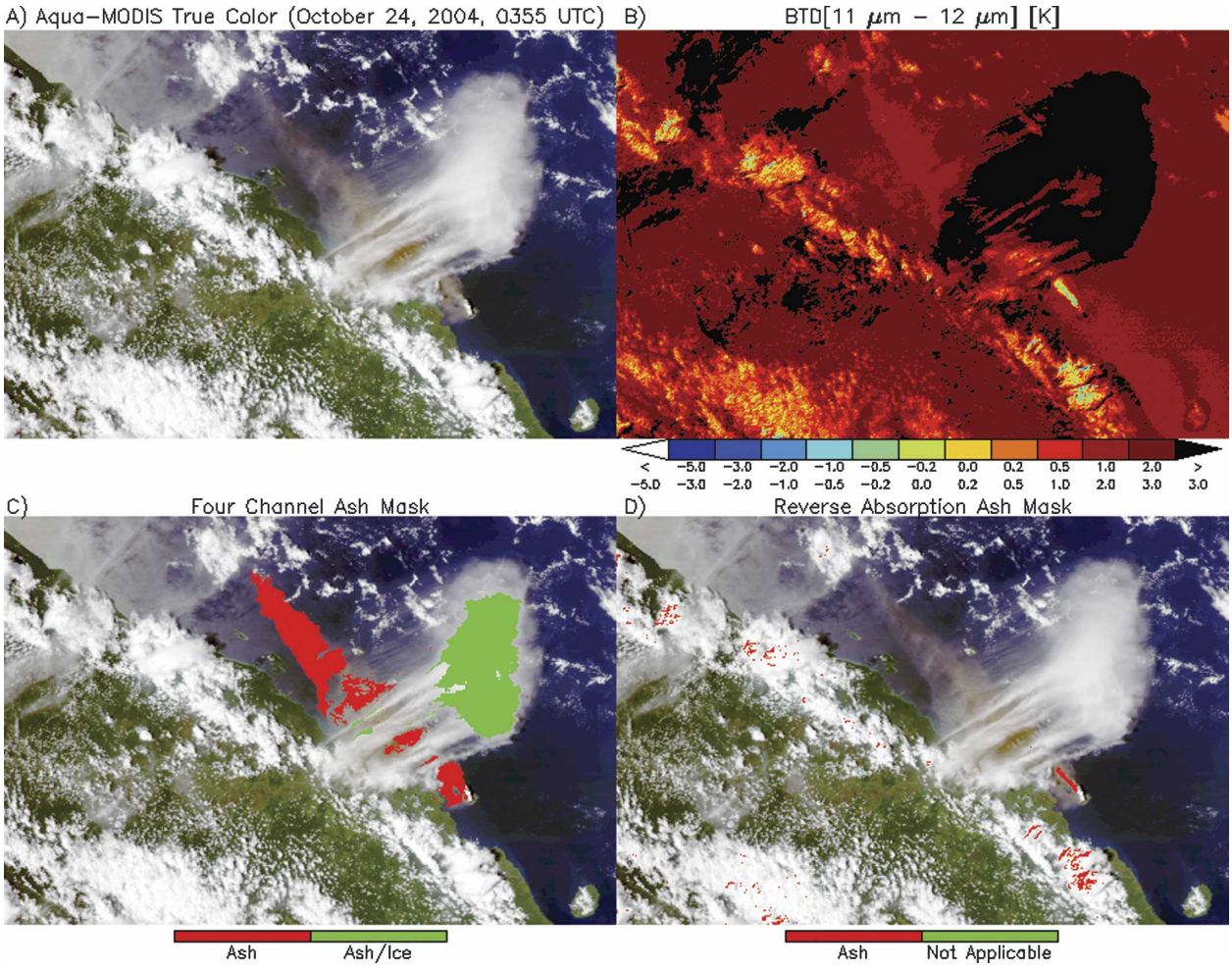

FIG. 4. An *Aqua* MODIS scene with a volcanic cloud produced from an eruption of Manam, PNG. The image is from 24 Oct 2004 at 0355 UTC. The (a) 1-km true color image created using the 0.65-, 0.56-, and 0.47-μm channels; (b) color-enhanced 11–12-μm brightness temperature difference image; (c) same as in (a), except the results of the four channel volcanic cloud detection algorithm are overlaid; and (d) same as in (a), except the results of the reverse absorption detection algorithm are overlaid.

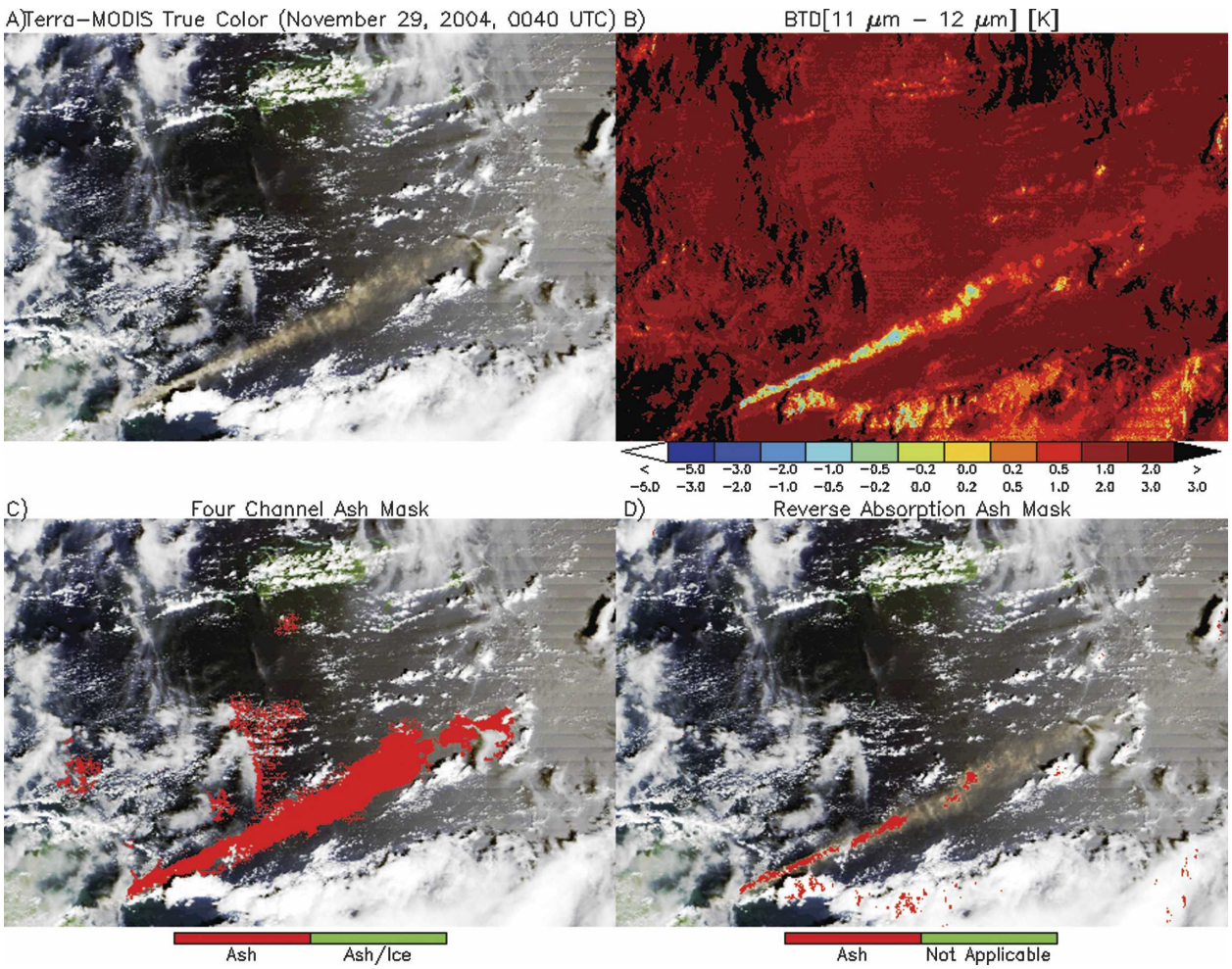

FIG. 5. Same as in Fig. 4, except from *Terra* MODIS on 29 Nov 2004 at 0040 UTC.

tober 2004 Manam case in that most of the volcanic cloud [estimated to be at a maximum height of about 4600 m by the Darwin VAAC (available online at http://www.bom.gov.au/info/vaac/advisories.shtml)] is not obscured by meteorological cloud. The BTD[11, 12] also shows that a much larger portion of the volcanic cloud produces a negative value, thus the reverse absorption technique does fairly well in optically thicker areas. Some convective clouds also produce a negative BTD[11, 12] as well. The new four-channel algorithm is able to detect even the very thin sections of the volcanic cloud (where BTD[11, 12] $>$ 1 K), even in sun glint regions. Cloud edges near cirrus are responsible for nearly all of the false alarms. These false alarms were mainly triggered by tier III tests. In this case, the new algorithm is able to detect much more of the volcanic cloud than the reverse absorption technique at the expense of some additional false alarms. It is important to point out that the added detection capabilities do not always correspond with an increase in false alarms (see example one above) compared to the reverse absorption technique. In addition, these false alarms could possibly be reduced by applying stricter post-spectral test spatial filters, or an analyst can simply view the results of the mask without the tier III test results if a "cleaner" though less complete volcanic cloud mask is desired. However, the complete mask shown here is important for retrieving other properties such as height, optical depth, and particle size.

c. Scene 3: Klyuchevskoy, Russia (8 March 2005)

The third scene captures an eruption of Klyuchevskoy on the Kamchatka Peninsula, Russia with *Terra* MODIS on 8 March 2005 at 0055 UTC (see Fig. 6). This scene is different from the others in that a large part of volcanic cloud is located over snow, which limits the effectiveness of any RAT[3.75, 0.65] tests. Despite the difficult background conditions, the

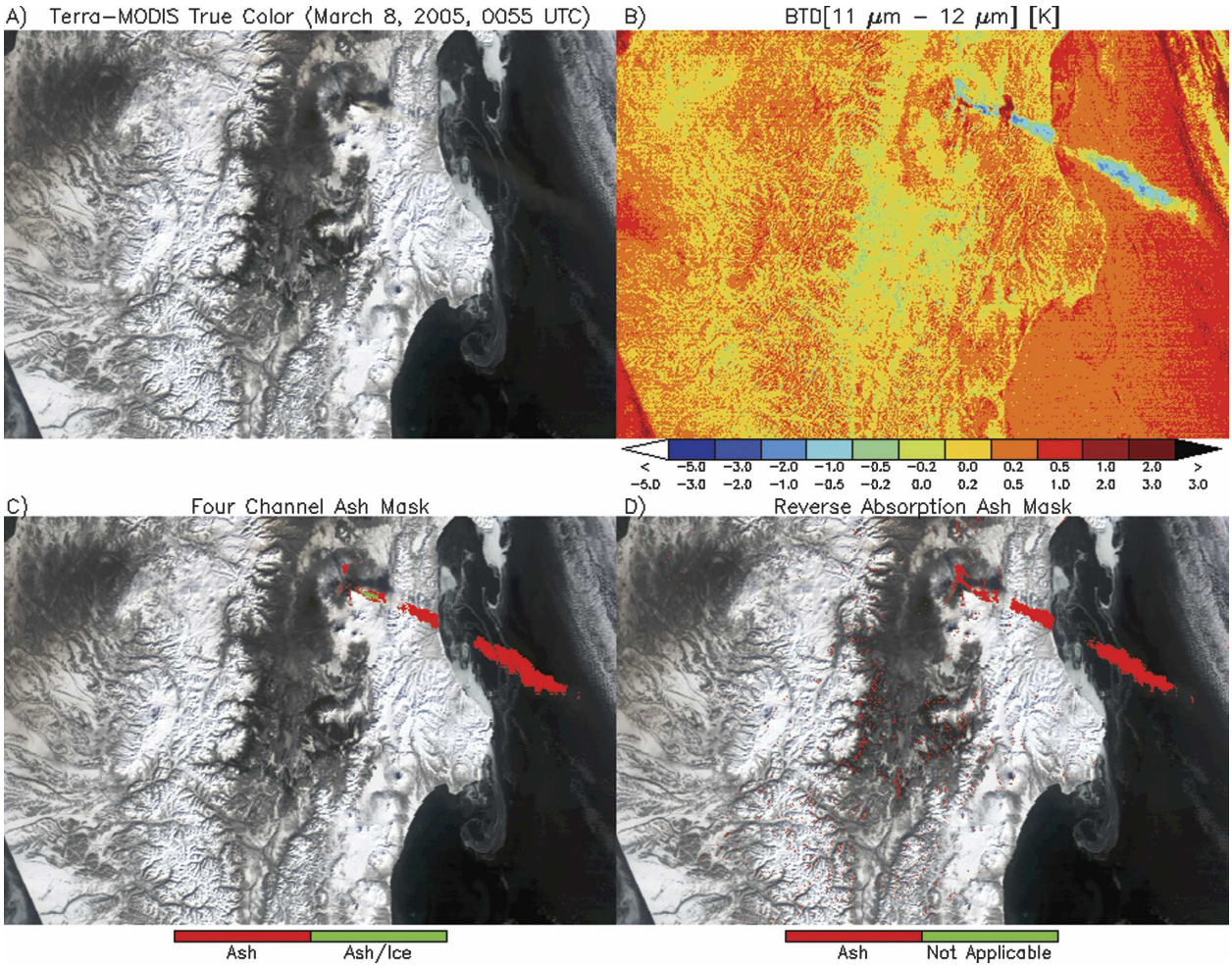

FIG. 6. Same as in Fig. 4, except for Klyuchevskoy, Russia, from *Terra* MODIS on 8 Mar 2005 at 0055 UTC.

four-channel algorithm is able to identify most of the visible volcanic cloud while generating very few false alarms. The reverse absorption algorithm also detects much of the cloud but with more false positives. Notice that near the coastline, the cloud becomes nearly invisible in the imagery and, as a result, is not detected by either algorithm. The volcanic cloud is then once again detected by both algorithms over open water. This case illustrates that even when the reverse absorption algorithm is effective, the new four-channel algorithm is just as effective, so there appears to be no loss in performance by implementing the new algorithm on volcanic clouds that are readily detected with the reverse absorption technique alone.

d. Scene 4: Mount Spurr, Alaska (19 August 1992)

Regardless of false alarms, the reverse absorption technique is most often able to effectively detect volcanic clouds in the high latitudes. Exceptions do occur though. For instance, much of the volcanic cloud associated with the explosive 19 August 1992 eruption of Mount Spurr, Alaska, was not able to be detected initially by the reverse absorption technique, although the cloud was later tracked very nicely for several days using reverse absorption (e.g., Schneider et al. 1995). The 1-km image shown in Fig. 7 is from the AVHRR on NOAA-11 at 0126 UTC, which is about 1.5 h after the start of the eruption. Shortly after the start of the eruption, AVHRR data indicated that most of the Mount Spurr cloud did not have a negative BTD[11, 12] (see Fig. 7b); it did, however, have a very distinct R[3.75] signal for such a cold target. Thus, the four-channel algorithm is quite useful for immediately and unambiguously detecting this cloud. The initial absence of a negative BTD[11, 12] signal was likely caused by the large cloud optical depth and/or the presence of ice/ash aggregates. Nevertheless, this scene illustrates that the new algorithm will not only produce less false alarms in

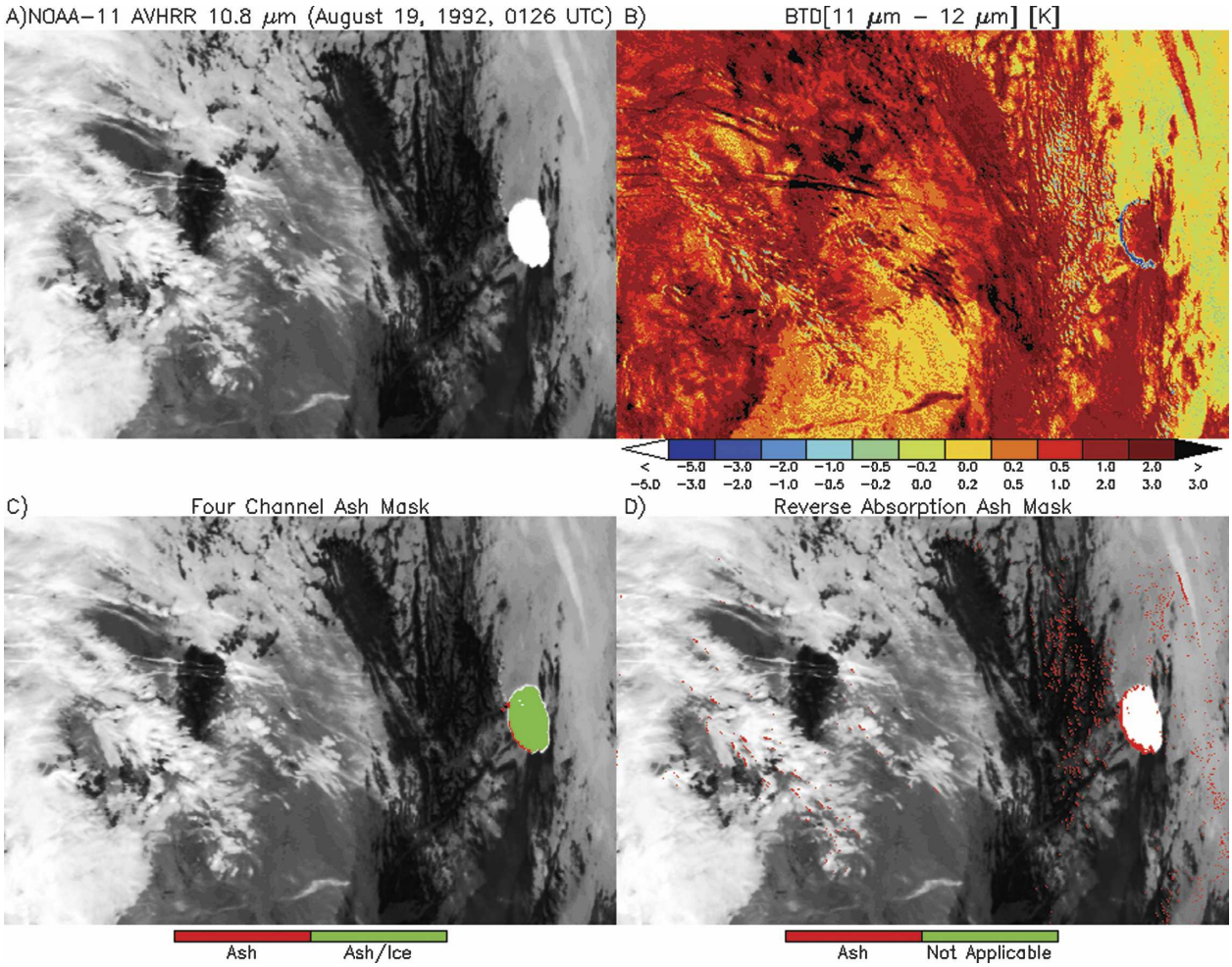

FIG. 7. Similar to Fig. 4, except a 10.8-μm image is substituted for the true color image. This *NOAA-11* AVHRR image shows the 19 Aug 1992 eruption of Mount Spurr, Alaska, at 0126 UTC.

the high latitudes than the reverse absorption algorithm, but it will also be less prone to missing the occasional volcanic cloud that does not have a distinct reverse absorption signal. In addition, this AVHRR scene was processed using the exact version of the four-channel algorithm that was applied to the MODIS data, illustrating that the algorithm can be readily applied to various sensors with similar channels.

e. Scene 5: Eastern Atlantic Ocean (16 May 2005)

The final example is used to show that the new algorithm is not sensitive to nonvolcanic mineral dust. This *Aqua* MODIS scene from 16 May 2005 at 1420 UTC shows a large dust cloud over the eastern Atlantic Ocean that originated from the African continent (see Fig. 8). Since this region is not located very close to any active volcanoes, it is assumed that the only detectable aerosol in this scene is nonvolcanic dust. Figure 8 shows that the new four-channel algorithm produces essentially no false alarms even though the BTD[11, 12] is <0.0 K throughout the dust cloud. The information from the BT[11] and the RAT[3.65, 0.65] effectively prevents these negative BTD[11, 12] pixels from being mistaken for volcanic ash. This result is important since nonvolcanic dust clouds may be present in regions of volcanic activity. For instance, prevailing winds often advect Saharan dust clouds into the Caribbean (Dunion and Velden 2004) where there are active volcanoes (e.g., Soufriere Hills, Montserrat). If only the reverse absorption technique is relied on, it is not possible to differentiate between volcanic dust and nonvolcanic dust. Simpson et al. (2003) explore this issue in further detail.

6. Global false alarm rate analysis

Not only is it important to examine various scenes that contain a volcanic cloud, it is equally important to

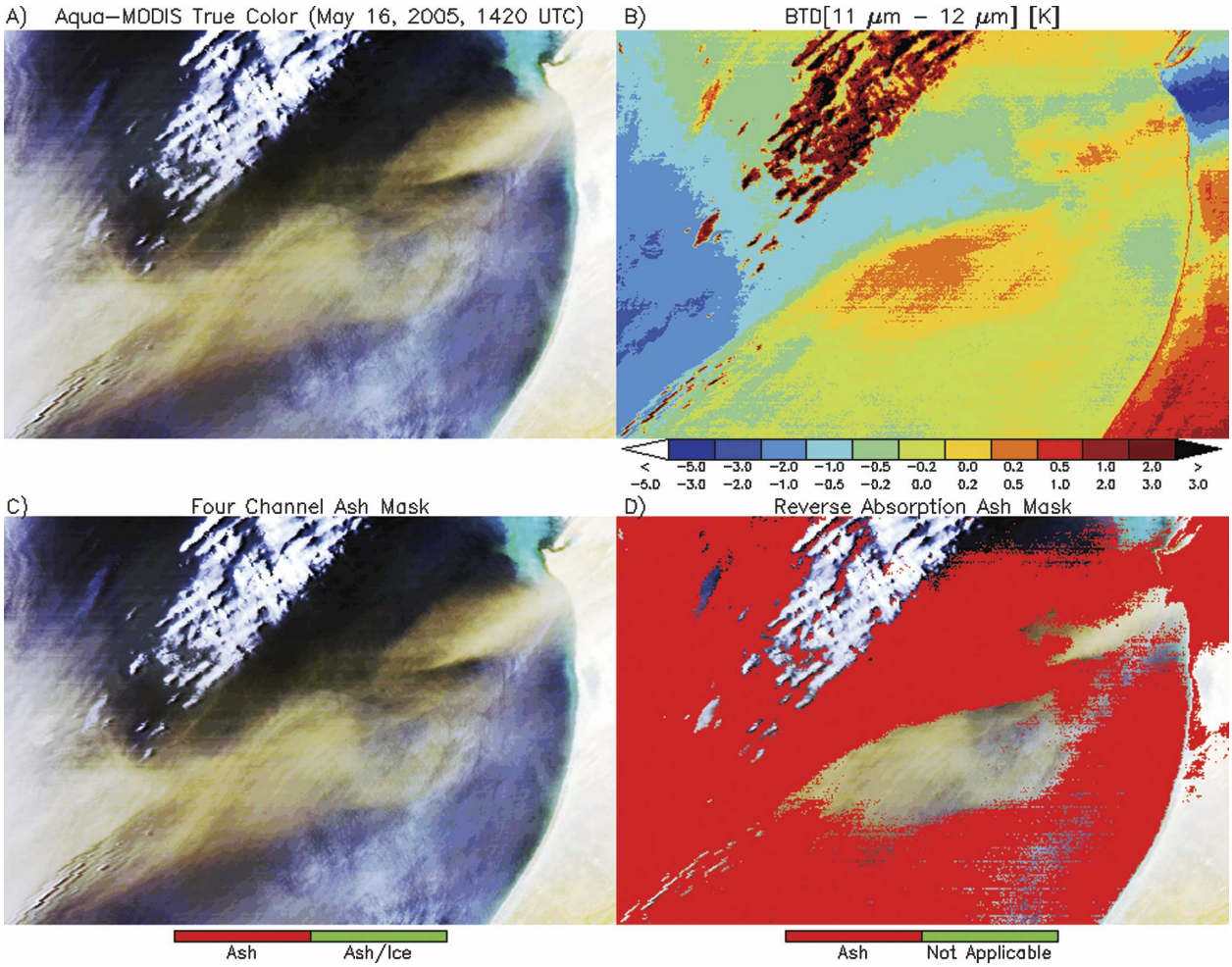

FIG. 8. Same as in Fig. 4, except for a Saharan dust cloud over the Atlantic Ocean off of the west coast of Africa from *Aqua* MODIS on 16 May 2005 at 1420 UTC.

examine many additional scenes that do not have ash present, and to do so on a global basis, in order to better characterize the false alarm rate of the algorithm. To perform this task, an entire day of descending node (mostly daytime observations) *Terra* MODIS data were processed for 4 April 2003. This date was chosen since only very weak and low-level gaseous emissions were reported to be emanating from a few volcanoes, and no significant activity was reported in the days preceding 4 April (see the Smithsonian/United States Geological Survey weekly report available online at http://www.volcano.si.edu/reports/usgs/). Our version (see section 5) of the reverse absorption technique was also applied to serve as a standard reference. Neither the reverse absorption nor the four-channel algorithm are particularly sensitive to very minor volcanic emissions, so if both automated algorithms were perfect, no volcanic clouds should be detected by either algorithm. Of course, no algorithm is perfect, so there will be false alarms. The important thing is that the false alarms are minimized and any that remain are understood and characterized. A full day of global data contains many different types of scenes, each with its own challenges.

Figure 9 shows the fraction of MODIS 1-km pixels within a 0.5° equal area box that were classified as a volcanic cloud by the four-channel algorithm. Figure 9 is not meant to be a product, just a diagnostic. Figure 10 is the same as Fig. 9, except that only the reverse absorption technique was applied. Keep in mind that this version of the reverse absorption algorithm does not necessarily represent any algorithm used in operations, as each operational center uses its own reverse absorption technique thresholds and filters. The four-channel algorithm produces only sporadic, generally low-magnitude, false alarms. When the false alarm producing regions shown in Fig. 9 were examined at the pixel

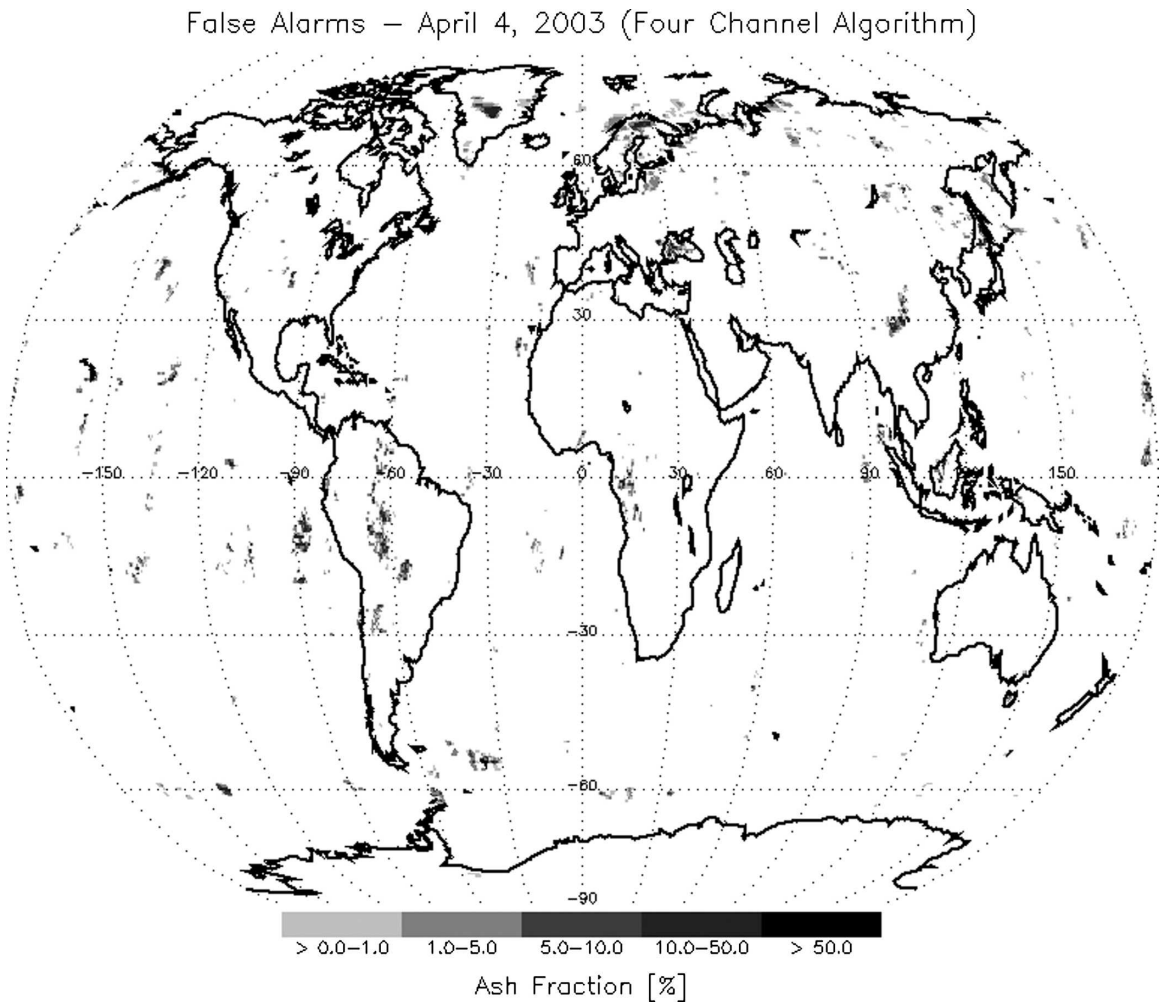

FIG. 9. The fraction of *Terra* MODIS 1-km pixels within a 0.5° equal area grid box that was classified as a volcanic cloud by the four-channel algorithm. Results from all of the descending node granules on 4 Apr 2003 are shown. This image is an indicator of false alarm rate since no volcanic eruptions were reported on this day or the previous few days.

level, we determined that the majority of the false alarms were caused by the RAT[3.75, 0.65] test used in tier II of the algorithm because of the edges of liquid water clouds. This outcome is not surprising given the information inferred from the single scatter albedo. In contrast, the reverse absorption algorithm produces numerous false alarms, which are physically consistent with the split window behavior as explained in detail in section 1 (e.g., deserts, cold cloud tops, temperature inversions, etc.). In practice, some of the reverse absorption false alarms can be easily eliminated by using a basic spatial filter and eliminating very warm features (e.g., deserts), but many false alarms would still remain, especially in the high latitudes.

Globally, 0.06% and 5.62% of the total number of pixels tested positive for volcanic clouds using the four-channel algorithm and reverse absorption algorithms, respectively. These results indicate that despite using several spectral tests (each of which has a risk of generating false alarms) in the four-channel algorithm, the overall false alarm rate is lower than the two channel reverse absorption technique false alarm rate. Thus, even though the false alarm rate of each algorithm was fairly similar in the Klyuchevskoy scene examined in section 5, the four-channel algorithm will produce significantly less false alarms over the course of many scenes. In summary, not only was the overall sensitivity to the presence of volcanic clouds increased by using the four-channel algorithm as opposed to our straightforward version of the reverse absorption algorithms, but the overall sensitivity to nonvolcanic features was decreased as well.

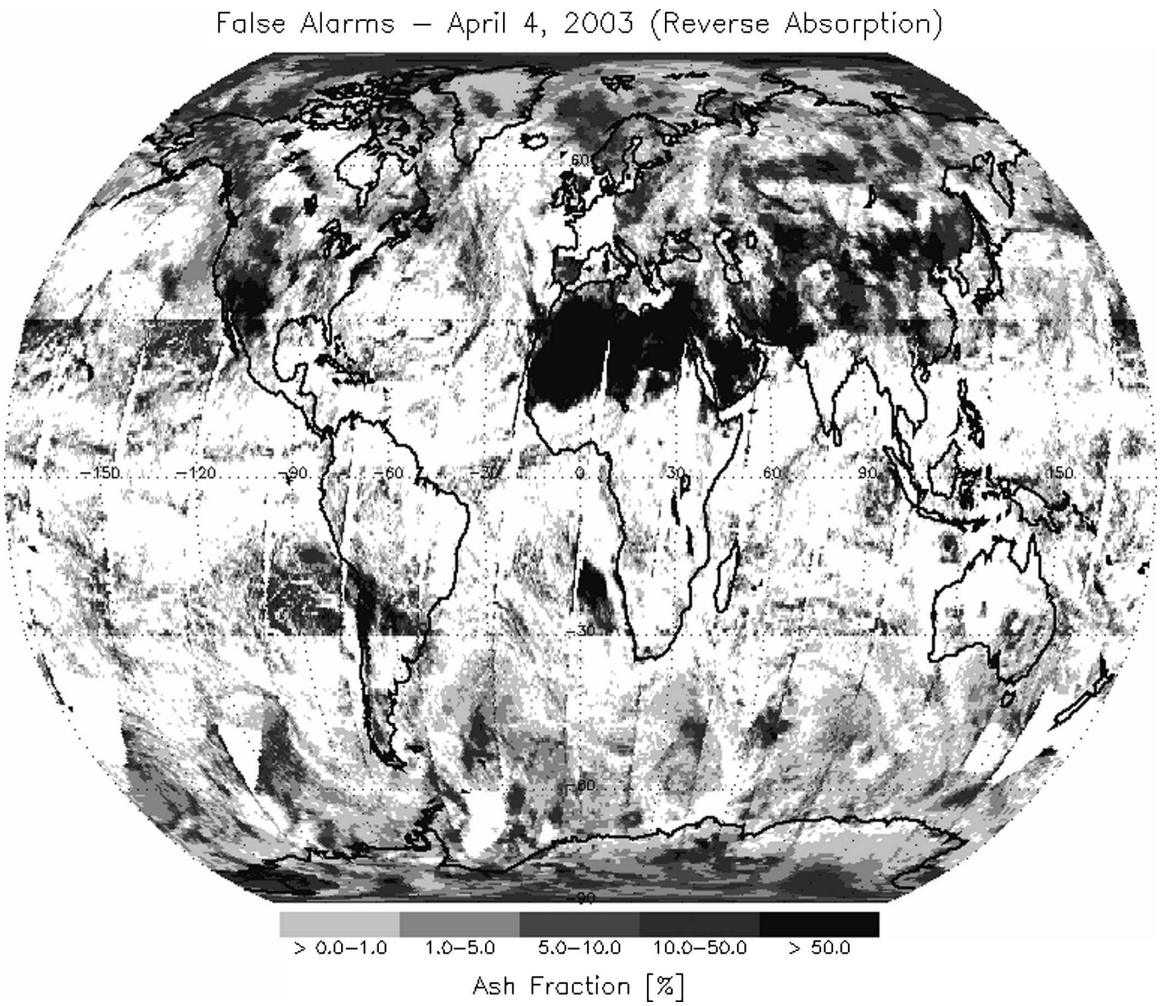

FIG. 10. The same as in Fig. 9, except the reverse absorption algorithm was used.

7. Conclusions

A volcanic cloud detection algorithm that utilizes four spectral channels (0.65, 3.75, 11, and 12 μm) that are common among several satellite-based instruments was presented in this paper. The results of this new algorithm were compared to a threshold-based reverse absorption algorithm, where the reverse absorption algorithm is used to identify measurements with a negative 11–12-μm brightness temperature difference. The purpose of this paper was not to criticize the reverse absorption technique, but rather to illustrate an alternative, more robust approach for using the important information given by the 11–12-μm brightness temperature difference. Furthermore, the algorithm presented here is not meant to be a substitute for qualitative techniques used by trained analysts but rather a value-added product that can provide additional quick and reliable information that can be used to improve near-real-time volcanic ash hazard assessments. An accurate and complete volcanic cloud mask is also needed as input into automated volcanic cloud height, particle size, and optical depth retrieval algorithms. These properties can then be used to improve volcanic cloud dispersion forecasts. Our results indicate that the new four-channel algorithm is not only more sensitive to the presence of volcanic aerosols but also generally less prone to false alarms than the standard reverse absorption algorithm. The greatest impact on detection sensitivity is seen in the Tropics, where water vapor can often mask the reverse absorption signal. The four-channel algorithm was able to detect volcanic clouds even when the 11–12-μm brightness temperature difference was greater than +2 K. In the higher latitudes, the greatest impact seen was the significant reduction in false alarms compared to the reverse absorption algorithm and the improved ability to detect optically thick volcanic clouds. Cloud water can also mask the reverse

absorption signal. The four-channel algorithm was shown to be more sensitive to volcanic clouds that have a water (ice or liquid water) component than the reverse absorption algorithm. The new algorithm should also be more effective at detecting volcanic clouds that reside in the lower stratosphere.

In this manuscript, mainly MODIS data were used, but the algorithm is applicable to many more sensors such as the AVHRR (as was shown in section 5d) and MTSAT. Based on previous work with multiplatform cloud typing algorithms (e.g., Pavolonis and Heidinger 2004; Pavolonis et al. 2005), only minimal adjustments should be necessary when applying the algorithm to other sensors to account for differences in horizontal resolution and spectral band characteristics. This algorithm is computationally efficient and requires no ancillary data, so its operational implementation is straightforward. Current instruments like MODIS and SEVIRI offer an even better opportunity to detect volcanic clouds, especially at night, and future sensors such as the Advanced Baseline Imager (ABI) on the GOES-R platform (2013) and the Visible/Infrared Imager/Radiometer Suite on the NPOESS platform (2008) will also offer additional operational capabilities. Future work will also focus on utilizing these additional capabilities for automated ash detection during the day and night. The daytime "tiered" detection philosophy can be applied to infrared channels to improve nighttime detection. It is also possible that in the future, the best approach to generating an automated volcanic aerosol mask will be to combine information from narrow bank imagers and hyperspectral infrared sounders. The hyperspectral sounder may provide a means to better detect subvisible volcanic clouds and/or volcanic clouds composed of mainly SO_2 and H_2SO_4. The MODIS/AIRS combination can be used to develop these algorithms in preparation for the Hyperspectral Environmental Suite (HES) and the Advanced Baseline Imager on the GOES-R platform, which is roughly scheduled for launch in 2013.

Acknowledgments. The authors thank Gary Ellrod and Andrew Tupper for many insightful conversations on volcanic ash detection. The MODIS data were obtained from the National Aeronautics and Space Administration (NASA) Distributed Active Archive Center (DAAC). This work was supported by the NASA Applied Sciences Program and the NASA Aviation Safety and Security Program through the NASA Advanced Satellite Aviation-weather Products (ASAP) project. The views, opinions, and findings contained in this paper are those of the authors and should not be construed as official National Oceanic and Atmospheric Administration or U.S. Government positions, policies, or decisions.

REFERENCES

Bonfiglio, A., M. Macchiato, N. Pergola, C. Pietrapertosa, and V. Tramutoli, 2005: AVHRR automated detection of volcanic clouds. *Int. J. Remote Sens.,* **26,** 9–28.

Briegleb, B. P., P. Minnis, V. Ramanathan, and E. Harrison, 1986: Comparison of regional clear-sky albedos inferred from satellite observations and model computations. *J. Climate Appl. Meteor.,* **25,** 214–226.

Downing, H. D., and D. Williams, 1975: Optical constants of water in the infrared. *J. Geophys. Res.,* **80,** 1656–1661.

Dunion, J. P., and C. S. Velden, 2004: The impact of the Saharan Air Layer on Atlantic tropical cyclone activity. *Bull. Amer. Meteor. Soc.,* **85,** 353–365.

Ellrod, G. P., 2004: Impact on volcanic ash detection caused by the loss of the 12.0-μm "split window" band on GOES imagers. *J. Volcanol. Geotherm. Res.,* **135,** 91–103.

——, and A. J. Schreiner, 2004: Volcanic ash detection and cloud top height estimates from the GOES-12 imager: Coping without a 12-μm infrared band. *Geophys. Res. Lett.,* **31,** L15110, doi:10.1029/2004GL020395.

——, B. H. Connell, and D. W. Hillger, 2003: Improved detection of airborne volcanic ash using multispectral infrared satellite data. *J. Geophys. Res.,* **108,** 4356, doi:10.1029/2002JD002802.

Fromm, M. D., and R. Servranckx, 2003: Transport of forest fire smoke above the tropopause by supercell convection. *Geophys. Res. Lett.,* **30,** 1542, doi:10.1029/2002GL016820.

Gosse, S., D. Labrie, and P. Chylek, 1995: Refractive index of ice in the 1.4–7.8 μm spectral range. *Appl. Opt.,* **34,** 6582–6586.

Guo, S., W. I. Rose, G. J. S. Bluth, and I. M. Watson, 2004: Particles in the great Pinatubo volcanic cloud of June 1991: The role of ice. *Geochem. Geophys. Geosyst.,* **5,** Q05003, doi:10.1029/2003GC000655.

Hansen, J. E., and J. B. Travis, 1974: Light scattering in planetary atmospheres. *Space Sci. Rev.,* **16,** 527–610.

Heidinger, A. K., R. Frey, and M. Pavolonis, 2004: Relative merits of the 1.6 and 3.75 μm channels of the AVHRR/3 for cloud detection. *Can. J. Remote Sens.,* **30,** 182–194.

Higurashi, A., and T. Nakajima, 2002: Detection of aerosol types over the East China Sea near Japan from four-channel satellite data. *Geophys. Res. Lett.,* **29,** 1836, doi:10.1029/2002GL015357.

Hufford, G. L., L. J. Salinas, J. J. Simpson, E. G. Barske, and D. C. Prieri, 2000: Operational implications of airborne volcanic ash. *Bull. Amer. Meteor. Soc.,* **81,** 745–755.

Key, J. R., and A. J. Schweiger, 1998: Tools for atmospheric radiative transfer: Streamer and FluxNet. *Comput. Geosci.,* **24,** 443–451.

——, and J. M. Intrieri, 2000: Cloud particle phase determination with the AVHRR. *J. Appl. Meteor.,* **39,** 1797–1804.

Kinoshita, K., C. Kanagaki, A. Minaka, S. Tsuchida, T. Matsui, A. Tupper, H. Yakiwara, and N. Iino, 2004: Ground and satellite monitoring of volcanic aerosols in visible and infrared bands. *Proc. Int. Symp. on Remote Sensing–Monitoring of Environmental Change in Asia,* Chiba, Japan, CERES, 1–10.

Miller, T. P., and T. J. Casadevall, 2000: Volcanic ash hazards to aviation. *Encyclopedia of Volcanoes,* H. Sigurdsson, Ed., Academic Press, 915–930.

Muñoz, O., H. Volten, J. W. Hovenier, B. Veihelmann, W. J. van der Zande, L. B. F. M. Waters, and W. I. Rose, 2004: Scat-

tering matrices of volcanic ash particles of Mount St. Helens, Redoubt, and Mount Spurr volcanoes. *J. Geophys. Res.,* **109,** D16201, doi:10.1029/2004JD004684.

Nasiri, S. L., B. A. Baum, A. J. Heymsfield, P. Yang, M. R. Poellot, D. P. Kratz, and Y. X. Hu, 2002: The development of midlatitude cirrus models for MODIS using FIRE-I, FIRE-II, and ARM in situ data. *J. Appl. Meteor.,* **41,** 197–217.

Neal, C. A., R. G. McGimsey, C. A. Gardner, M. L. Harbin, and C. J. Nye, 1994: Tephra-fall deposits from 1992 eruptions of Crater Peak, Mount Spurr Volcano, AK: A preliminary report on distribution, stratigraphy, and composition. The 1992 eruptions of Crater Peak vent, Mount Spurr volcano, Alaska, U.S. Geological Survey Bulletin 2139, 65–79.

Pavolonis, M. J., and A. K. Heidinger, 2004: Daytime cloud overlap detection from AVHRR and VIIRS. *J. Appl. Meteor.,* **43,** 762–778.

——, ——, and T. Uttal, 2005: Daytime global cloud typing from AVHRR and VIIRS: Algorithm description, validation, and comparisons. *J. Appl. Meteor.,* **44,** 804–826.

Pergola, N., V. Tramutoli, F. Marchese, I. Scaffidi, and T. Lacava, 2004: Improving volcanic ash cloud detection by a robust satellite technique. *Remote Sens. Environ.,* **90,** 1–22.

Pollack, J. B., O. B. Toon, and B. N. Khare, 1973: Optical properties of some terrestrial rocks and glasses. *Icarus,* **19,** 372–389.

Prata, A. J., 1989a: Observations of volcanic ash clouds in the 10–12-micron window using AVHRR/2 Data. *Int. J. Remote Sens.,* **10,** 751–761.

——, 1989b: Radiative transfer calculations for volcanic ash clouds. *Geophys. Res. Lett.,* **16,** 1293–1296.

——, G. J. S. Bluth, W. I. Rose, D. J. Schneider, and A. C. Tupper, 2001: Comments on "Failures in detecting volcanic ash from a satellite-based technique." *Remote Sens. Environ.,* **78,** 341–346.

Riley, C. M., W. I. Rose, and G. J. S. Bluth, 2003: Quantitative shape measurements of distal volcanic ash. *J. Geophys. Res.,* **108,** 2504, doi:10.1029/2001JB000818.

Rose, W. I., and Coauthors, 1995: Ice in the 1994 Rabaul eruption cloud-implications for volcano hazard and atmospheric effects. *Nature,* **375,** 477–479.

——, G. J. S. Bluth, D. J. Schneider, G. G. J. Ernst, C. M. Riley, L. J. Henderson, and R. G. McGimsey, 2001: Observations of volcanic clouds in their first few days of atmospheric residence: The 1992 eruptions of Crater Peak, Mount Spurr volcano, Alaska. *J. Geol.,* **109,** 677–694.

——, and Coauthors, 2003: The February–March 2000 eruption of Hekla, Iceland from a satellite perspective. *Volcanism and the Earth's Atmosphere, Geophys. Monogr.,* Vol. 139, Amer. Geophys. Union, 107–132.

Schneider, D. J., W. I. Rose, and L. Kelley, 1995: Tracking of 1992 eruption clouds from Crater Peak Vent of Mount Spurr Volcano, Alaska, using AVHRR. U.S. Geological Survey Bulletin 2139, 27–36.

Seemann, S. W., J. Li, W. P. Menzel, and L. E. Gumley, 2003: Operational retrieval of atmospheric temperature, moisture, and ozone from MODIS infrared radiances. *J. Appl. Meteor.,* **42,** 1072–1091.

Sherwood, S. C., 2002: Aerosols and ice particle size in tropical cumulonimbus. *J. Climate,* **15,** 1051–1063.

Simpson, J. J., G. Hufford, D. Pieri, and J. Berg, 2000: Failures in detecting volcanic ash from a satellite-based technique. *Remote Sens. Environ.,* **72,** 191–217.

——, G. L. Hufford, R. Servranckx, J. S. Berg, and D. Pieri, 2003: Airborne Asian dust: Case study of long-range transport and implications for the detection of volcanic ash. *Wea. Forecasting,* **18,** 121–141.

Sokolik, I. N., and O. B. Toon, 1999: Incorporation of mineralogical composition into models of the radiative properties of mineral aerosol from UV to IR wavelengths. *J. Geophys. Res.,* **104,** 9423–9444.

Sun, Z., and K. P. Shine, 1995: Parameterization of ice cloud radiative properties and its application to the potential climatic importance of mixed-phase clouds. *J. Climate,* **8,** 1874–1888.

Textor, C., H. F. Graf, M. Herzog, J. M. Oberhuber, W. I. Rose, and G. G. J. Ernst, 2006a: Volcanic particle aggregation in explosive eruptive columns. Part I: Parameterization of the microphysics of hydrometeors and ash. *J. Volcanol. Geotherm. Res.,* **150,** 359–377.

——, ——, ——, ——, ——, and ——, 2006b: Volcanic particle aggregation in explosive eruptive columns. Part II: Numerical experiments. *J. Volcanol. Geotherm. Res.,* **150,** 378–394.

Tsay, S.-C., and G. L. Stephens, 1990: A physical/optical model for atmospheric aerosols with application to visibility problems. Tech. Doc., 65 pp.

Tupper, A., and K. Kinoshita, 2003: Satellite, air, and ground observations of volcanic clouds over islands of the Southwest Pacific. *S. Pacific Study,* **23** (2), 21–46.

——, S. Carn, J. Davey, Y. Kamada, R. Potts, F. Prata, and M. Tokuno, 2004: An evaluation of volcanic cloud detection techniques during recent significant eruptions in the western 'Ring of Fire.' *Remote Sens. Environ.,* **91,** 27–46.

——, J. S. Oswalt, and D. Rosenfeld, 2005: Satellite and radar analysis of the volcanic-cumulonimbi at Mount Pinatubo, Philippines, 1991. *J. Geophys. Res.,* **110,** D09204, doi:10.1029/2004JD005499.

Turner, D. D., S. A. Ackerman, B. A. Baum, H. E. Revercomb, and P. Yang, 2003: Cloud phase determination using ground-based AERI observations at SHEBA. *J. Appl. Meteor.,* **42,** 701–715.

Warren, S., 1984: Optical constants of ice from the ultraviolet to the microwave. *Appl. Opt.,* **23,** 1206–1225.

Yu, T. X., W. I. Rose, and A. J. Prata, 2002: Atmospheric correction for satellite-based volcanic ash mapping and retrievals using "split window" IR data from GOES and AVHRR. *J. Geophys. Res.,* **107,** 4311, doi:10.1029/2001JD000706.